HORIZON EUROPE PROGRAMME
TOPIC HORIZON-CL4-2022-RESILIENCE-01-24

GA No. 101091572

Graphene, MXene and ionic liquid-based sustainable supercapacitor

GREENCAP - Deliverable report

D2.2. – Hybrids and functionalized EMs characterization

Funded by
the European Union

Deliverable No.	GREENCAP D2.1	
Related WP	WP 2	
Deliverable Title	Hybrids and functionalized EMs characterization	
Deliverable Date	2025-06-30	
Deliverable Type	REPORT	
Dissemination level	Public (PU)	
Author(s)	Artur Ciesielski (UNISTRA)	
Checked by	Paolo Samori (UNISTRA)	2025-06-14
Reviewed by (if applicable)	Alberto Morenghi (BED)	2025-06-25
Approved by	Francesco Bonaccorso (BED) - Project coordinator	2025-06-30
Status	Final	2025-06-30

Document History

Version	Date	Editing done by	Remarks
V01	2025-06-14	UNISTRA	
V02	2025-06-24	Alberto Morenghi (BED)	
V1.0	2025-06-30	Francesco Bonaccorso	final
V1.1			
V2.0			

Project summary

The aim of the GREENCAP project is revolutionization of energy storage area while at the same time strive towards the EU's climate-neutrality goals and the Action Plan on Critical Raw Materials (CRMs). This multi-disciplinary consortium, consisting of partners from eight European countries, pursues to develop sustainable electrode materials for supercapacitors (SCs) that display battery-like energy density, high power densities as well as long cycle life. By employing both graphene and MXenes as electrode materials and ionic liquids (ILs) for high-voltage electrolytes, GREENCAP will improve the material’s specific surface area, ion accessibility as well as charge storage, while ensuring stability and safety across a wide range of temperatures. Ultimately, the project will lead to validation of this SC technology at an industrial scale (TRL 6) and development of a management system to optimize SC integration into high-end applications and the circular economy.

Publishable summary

Deliverable D2.2 of the GREENCAP project presents key advances in the development and characterization of functionalized and hybrid electrode materials (EMs) for high-performance supercapacitors. This work supports the project's broader objective of enabling sustainable, CRM-free energy storage systems that combine high energy and power densities with long cycle life and operational safety across a wide temperature range.

The main focus of Work Package 2 (WP2) is on enhancing SC electrode performance by tailoring material interfaces through two main strategies: (i) the chemical functionalization of two-dimensional (2D) materials—including graphene derivatives and MXenes - and (ii) their hybridization to leverage complementary properties. Together, these approaches improve ion transport, charge storage mechanisms, and electrode stability. Additionally, ionic liquid (IL)-based systems, including ionogel (IG) electrodes, are explored as advanced electrolyte solutions and for their potential in improving processability and device safety.

A central result of this deliverable is the successful hybridization of reduced graphene oxide (rGO) with $Ti_3C_2T_x$ MXene, prepared via both physical mixing and covalent functionalization using (3-aminopropyl)triethoxysilane (APTES). The functionalization process creates stable chemical bonds, confirmed via X-ray photoelectron spectroscopy (XPS), between the two materials, enhancing conductivity, interfacial contact, and electrochemical activity. In parallel, diazonium chemistry (*e.g.,* 4-nitrobenzenediazonium tetrafluoroborate) was applied to graphene, while sulfonated azobenzene derivatives were used to functionalize V_2C MXene. These treatments increased the defect density and interlayer spacing, improving accessibility for electrolyte ions without compromising the electronic properties.

Another important result includes the hybridization of curved graphene (CG) with few-layer graphene (FLG). This approach combines the mechanical robustness and high surface area of CG with the conductivity and flexibility of FLG, producing electrodes with enhanced porosity, improved electrolyte diffusion, and increased capacitance stability. These hybrid systems are being optimized for scalability and performance in practical electrode formulations.

Complementing the work on hybrid EMs, the deliverable also reports progress on the development of ionogel-based electrodes. These systems are produced by incorporating ionic liquids—specifically 1-ethyl-3-methylimidazolium bis(fluorosulfonyl)imide (EMImFSI) and 1-propyl-3-methylimidazolium bis(fluorosulfonyl)imide (PMImFSI)—with activated carbon (AC), CG or MXene. The resulting IGs eliminate the need for volatile solvents and electrode drying, improving manufacturing safety and reducing the environmental impact. CG-based IG electrodes showed promising electrochemical stability and processability. While challenges were encountered in IL-prefilling of MXene-based electrodes, this work lays the groundwork for future optimization.

Overall, Deliverable D2.2 successfully achieves its objectives by advancing hybrid material formulations and functionalization techniques, while integrating ionic liquids as part of the broader electrode/electrolyte engineering strategy. These developments contribute directly to GREENCAP’s mission to produce CRM-free, scalable, and high-performance SC technologies for industrial applications and energy storage in a climate-resilient Europe.

Contents

List of Figures

List of Tables

Abbreviations & Definitions

Abbreviation	Explanation
2DMs	Two-dimensional materials
4NBD	4-Nitrobenzenediazonium tetrafluoroborate
AA	Ascorbic acid
AC	Activated carbon
AFM	Atomic force microscopy
AM	Active material
APTES	(3-Aminopropyl)triethoxysilane
ASA	4-aminoazobenzene-4'-sulfonic acid sodium salt
CG	Curved graphene
CMC/SBR	Carboxymethyl cellulose/styrene-butadiene rubber binder
CRMs	Critical raw materials
CV	Cyclic voltammetry
DSC	Differential scanning calorimetry
EDLC	Electric double layer capacitor
EDX	Energy-dispersive X-ray spectroscopy
EIHTFSI	1-ethylimidazolium bis(trifluoromethylsulfonyl)imide
EM	Electrode material
EMImFSI/EMIFSI	1-ethyl-3-methylimidazolium bis(fluorosulfonyl)imide
ESR	Equivalent series resistance
FLG	Few layers graphene
FT-IR	Fourier-transform infrared spectroscopy
GCD	Galvanostatic charge-discharge
GO	Graphene oxide
HR-TEM	High-resolution transmission electron microscopy
IG	Ionogels
IL	Ionic liquid
N1113FSI	N-trimethyl-N-propylammonium Bis(trifluoromethanesulfonyl)imide
PES	Photoemission spectroscopy
PTFE	polytetrafluoroethylene
PMImFSI	1-propyl-3-methylimidazolium bis(fluorosulfonyl)imide
PVDF	Polyvinylidene
$Pyr_{13}FSI$	N-propyl-N-methylpyrrolidinium bis(fluorosulfonyl)imide
rGO	Reduced graphene oxide
RT	Room temperature
SEM	Scanning electron microscopy
SCs	Supercapacitors
sota	State-of-the-art
TGA	Thermogravimetric analysis

WP	Work Package
XPS	X-ray photoelectron spectroscopy
XRD	X-ray diffraction

1 Introduction

Two-dimensional materials (2DMs), such as graphene derivatives and MXenes, have garnered considerable attention in the domain of electrochemical energy storage due to their exceptional physicochemical properties. These include high electrical conductivity, tunable surface chemistry, large specific surface area, tunable surface functionalities, and mechanical flexibility. Collectively, these characteristics position 2DMs as promising building blocks for next-generation supercapacitors (SCs), which are energy storage devices known for their high power density, rapid charge–discharge dynamics, and outstanding cycle stability.

A persistent challenge in the development of supercapacitor technologies lies in the enhancement of energy density without compromising power density or long-term operational stability. To address this, the GREENCAP project investigates the rational design and engineering of advanced electrode architectures based on functionalized and hybridized 2DMs. The extensive surface area of these materials provides abundant electrochemically active sites for electrical double-layer formation, while certain 2DMs, particularly MXenes, enable reversible ion intercalation within their lamellar structures, contributing additional pseudocapacitive charge storage. This synergy between electrical double-layer and pseudocapacitive mechanisms offers a compelling pathway toward improving both energy and power metrics in SCs.

Work Package 2 specifically aims to advance this concept through the tailored synthesis and structural optimization of hybrid and chemically functionalized 2DM-based electrodes. A key strategy involves the deliberate hybridization of distinct 2DMs to harness their complementary properties. For instance, reduced graphene oxide (rGO) exhibits high electrical conductivity and modifiable surface chemistry, while $Ti_3C_2T_x$ MXene provides a layered morphology conducive to efficient ion intercalation. The covalent functionalization and integration of these materials into composite systems are anticipated to enhance interfacial compatibility, structural integrity, and overall electrochemical performance.

A notable innovation presented in this deliverable is the exploration of hybrid systems that go beyond conventional rGO/MXene pairings. Specifically, curved graphene (CG) has been hybridized with few-layer graphene (FLG), combining CG’s high porosity and unique morphology with the excellent electronic conductivity and flexibility of FLG. These CG–FLG hybrid structures are engineered to facilitate superior electrolyte infiltration and promote rapid ion transport, thereby improving charge storage kinetics and cycling durability.

In parallel, the deliverable explores the use of ionic liquids (ILs) as advanced electrolytes to enhance electrode–electrolyte interfacial interactions while replacing volatile organic solvents with inherently safer, non-flammable alternatives. In this context, ionogel (IG) electrodes have been developed by incorporating ILs into AC, CG and MXene matrices. This approach enables the fabrication of solvent-free, ready-to-use electrode materials. ILs such as 1-ethyl-3-methylimidazolium *bis*(fluorosulfonyl)imide (EMIM-FSI) and 1-propyl-3-methylimidazolium *bis*(fluorosulfonyl)imide (PMIM-FSI) were systematically investigated for their electrochemical stability, processability, and integration compatibility. While CG-based IG electrodes demonstrated favorable mechanical properties and stable cycling performance, challenges persist in the processing and mechanical cohesion of IL-filled MXene electrodes, necessitating further material and process optimization.

Overall, the results outlined in this deliverable affirm the feasibility and promise of hybridized 2DM-based systems for the development of scalable, high-performance supercapacitors. The work underscores the critical role of molecular-level material engineering via surface functionalization and hybrid architecture design, and system-level optimization through advanced electrolyte integration in achieving the GREENCAP project's overarching goals of sustainable materials utilization, critical raw material (CRM) substitution, and circularity in energy storage technologies.

2 Preparation of rGO and $Ti_3C_2T_x$ MXene hybrids

UNISTRA prepared rGO+$Ti_3C_2T_x$ hybrids by first preparing rGO by chemical reduction using ascorbic acid (AA) as a reducing agent. $Ti_3C_2T_x$ MXene was supplied by CU. rGO+$Ti_3C_2T_x$ hybrids were obtained in two ways: (*i*) both materials were grinded together in a mortar using H_2O as a solvent, and (*ii*) rGO and $Ti_3C_2T_x$ MXene were stirred together in a round-bottom flask in H_2O at room temperature (RT) for 24 hours under N_2 atmosphere. After sonication, each solution was drop cast on a carbon paper electrode. The electrodes were ready for electrochemical measurements in three-electrode system after drying in a vacuum oven overnight at 80°C.

X-ray photoelectron spectroscopy (XPS) analysis was performed in order to confirm the preparation of rGO+$Ti_3C_2T_x$ hybrid. According to survey spectrum of rGO+$Ti_3C_2T_x$ hybrid after 24 hours of stirring (green graph, Figure 1 a), the material contains carbon (63.6 %), oxygen (16.3 %), titanium (10.6 %), fluorine (6.1 %), nitrogen (2.3 %), and chlorine (1.1 %; after exfoliation of $Ti_3C_2T_x$ MXene). The high-resolution C 1s spectrum of rGO+$Ti_3C_2T_x$ hybrid (Figure 1 f) confirmed the presence of peaks from both components, rGO and $Ti_3C_2T_x$ MXene, while according to Ti 2p spectra (Figure 1 b and c), there is no significant differences in $Ti_3C_2T_x$ before and after preparation of hybrid.

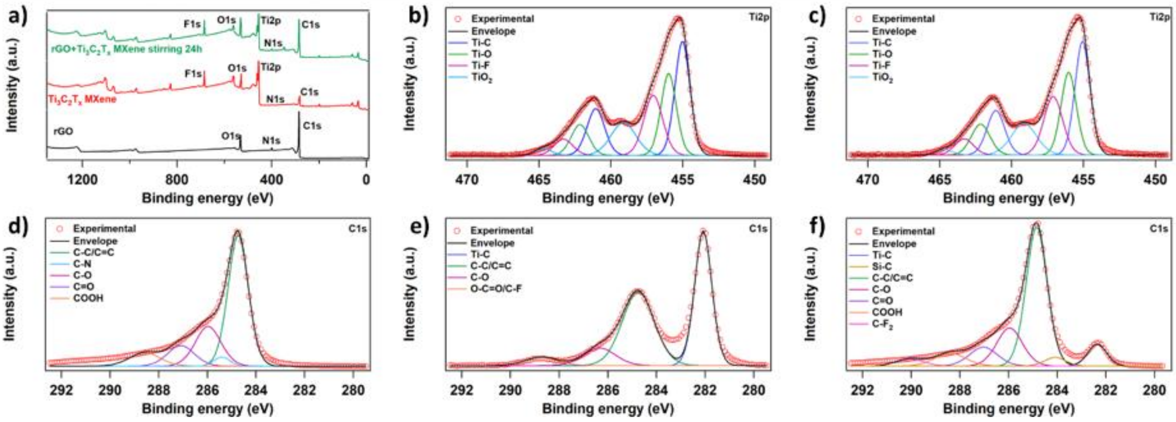

Figure 1. a) Comparison of XPS survey spectra of rGO, $Ti_3C_2T_x$ MXene, and rGO+$Ti_3C_2T_x$ MXene hybrid (stirring 24h). High-resolution XPS Ti 2p spectra of: b) $Ti_3C_2T_x$ MXene, c) rGO+ $Ti_3C_2T_x$ MXene. High-resolution XPS C 1s spectra of: d) rGO, e) $Ti_3C_2T_x$ MXene, and f) rGO+$Ti_3C_2T_x$ MXene.

The electrochemical characterization of these materials is included in the Deliverable 2.3. Electrochemical characterization of electrode/electrolyte interfaces.

3 Preparation of rGO and $Ti_3C_2T_x$ MXene hybrids with APTES

UNISTRA functionalized $Ti_3C_2T_x$ MXene with APTES *via* covalent bond formation between the silanol groups of the silanol coupling agent, after the hydrolysis reaction, and the hydroxyl groups present on the surface of MXene. On the other hand, graphene oxide (GO) as well as rGO, can undergo reaction with APTES by the epoxy ring opening of (r)GO with the amine groups present in APTES. Hence, APTES can act as a bridge connecting both (r)GO and $Ti_3C_2T_x$ MXene by the covalent bonds.

To prepare rGO+APTES+$Ti_3C_2T_x$ hybrids, UNISTRA prepared rGO by chemical reduction using AA. $Ti_3C_2T_x$ MXene was supplied by CU, while APTES was commercially purchased. rGO+APTES+$Ti_3C_2T_x$ hybrids were obtained as a result of one-pot reaction of rGO, APTES and $Ti_3C_2T_x$ MXene in ethanol at RT for 24 hours. Additionally, rGO+APTES as well as $Ti_3C_2T_x$+APTES hybrids were obtained under the same experimental conditions to collect all information and gain full view of all hybrid materials.

The Figure 2 displays the XPS survey spectra, while Table 1 presents the percentage composition of starting materials and prepared hybrids.

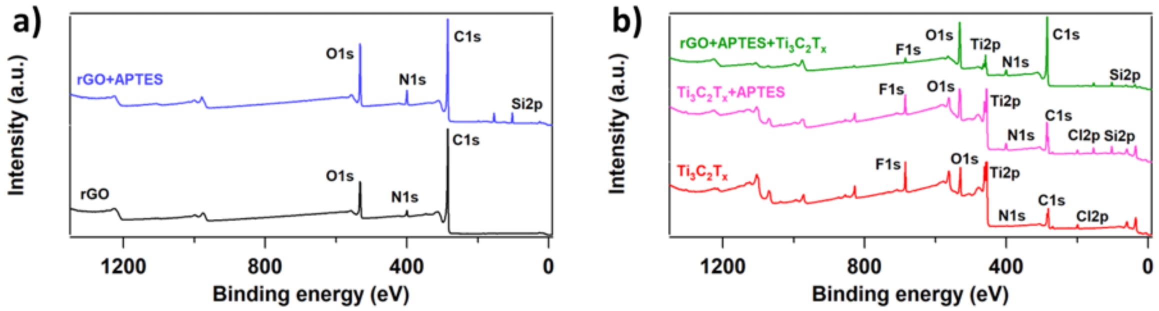

Figure 2. Comparison of XPS survey spectra of: a) rGO and rGO+APTES; b) $Ti_3C_2T_x$ MXene, $Ti_3C_2T_x$+APTES, and rGO+APTES+$Ti_3C_2T_x$.

Table 1. The percentage composition of rGO, $Ti_3C_2T_x$ and their hybrids with APTES based on XPS survey spectra.

Element	rGO	$Ti_3C_2T_x$	rGO+APTES	$Ti_3C_2T_x$+APTES	rGO+APTES+ $Ti_3C_2T_x$
C 1s	82.5%	36.4%	69.1%	42.7%	65.3%
O 1s	13.9%	18.0%	17.7%	20.9%	20.6%
N 1s	3.6%	1.3%	7.2%	6.0%	4.6%
Ti2p	-	29.7%	-	16.0%	4.6%
Si 2p	-	-	6.0%	6.6%	3.4%
F 1s	-	12.2%	-	6.1%	1.5%
Cl 2p	-	2.4%	-	1.7%	-

According to high-resolution C 1s XPS spectra of rGO+APTES, $Ti_3C_2T_x$+APTES, and rGO+APTES+$Ti_3C_2T_x$ hybrids (Figure 3 a-c), a new peak at ~283.8 eV is observed, that can be assigned to Si-C bond, indicating the successful functionalization of all materials with APTES. However, depending on the material, the percentage varies, being the lowest in rGO+APTES+$Ti_3C_2T_x$ hybrid. On the high-resolution Si 2p spectra (Figure 3 d-f), the peak at ~102.8 eV is visible, that can be assigned to Si-O-C bond, but depending on the hybrid, the width of the peak differs – 1.64, 1.8 and 1.9 for rGO+APTES, $Ti_3C_2T_x$+APTES, and rGO+APTES+$Ti_3C_2T_x$, respectively. Moreover, on the Ti 2p spectrum of $Ti_3C_2T_x$+APTES (Figure 3 g), there is no significant differences comparing to the starting material (Figure 1 b), in contrast to rGO+APTES+$Ti_3C_2T_x$ hybrid, where there is big increase in the peaks from TiO_2 (Figure 3 h), indicating partial oxidation of MXene component of hybrid.

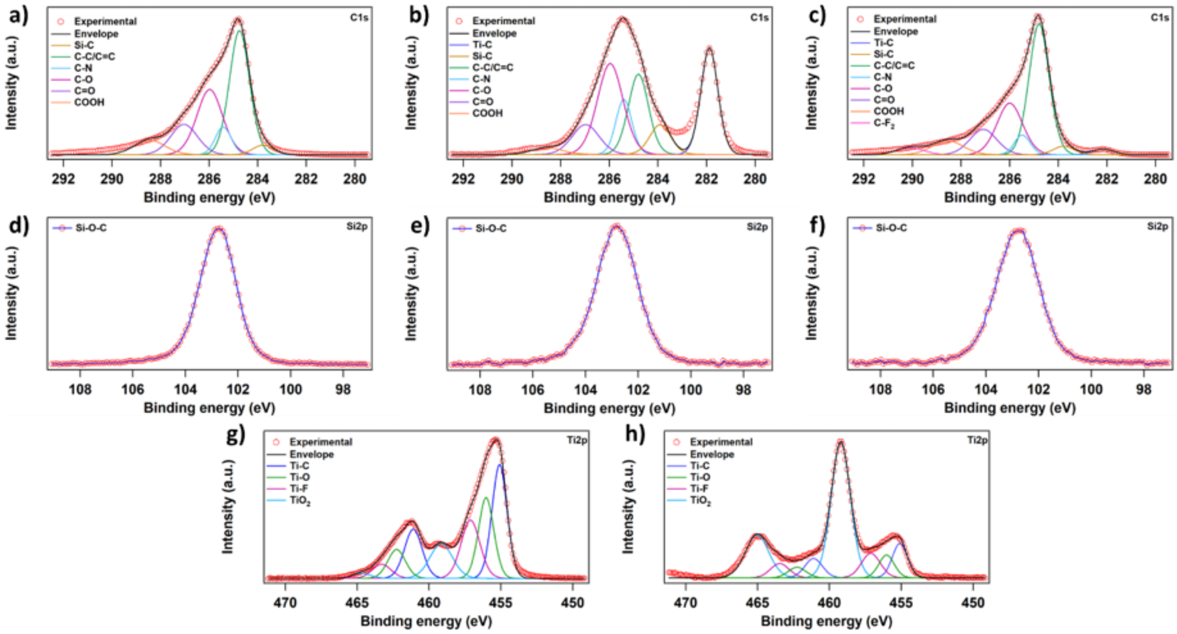

Figure 3. High-resolution XPS spectra of: a) C 1s rGO+APTES, b) C 1s $Ti_3C_2T_x$+APTES, c) C 1s rGO+APTES+$Ti_3C_2T_x$, d) Si 2p rGO+APTES, e) Si 2p $Ti_3C_2T_x$+APTES, f) Si 2p rGO+APTES+$Ti_3C_2T_x$, g) Ti 2p $Ti_3C_2T_x$+APTES, and h) Ti 2p rGO+APTES+$Ti_3C_2T_x$.

Moreover, in order to obtain an higher degree of functionalization with APTES, the use of GO, instead of rGO, has been assessed. In fact, GO possess an higher amount of oxygen groups and, consequentially, more sites available for the functionalization with APTES than rGO. All the hybrids with GO are prepared under the same experimental conditions. In addition, in order to obtain better electrochemical performance of these hybrids, the GO+APTES and GO+APTES+$Ti_3C_2T_x$ were heated in the vacuum oven at 140°C for 5 hours to trigger the reduction of GO and therefore boost the electrical conductivity of the hybrid material.

Table 2. The percentage composition of GO+APTES and GO+APTES+$Ti_3C_2T_x$ before and after heating based on XPS survey spectra. "T" means heating at 140°C in the vacuum oven.

Element	GO+APTES	GO+APTES T	GO+APTES+ $Ti_3C_2T_x$	GO+APTES+ $Ti_3C_2T_x$ T
C 1s	61.1%	63.1%	58.8%	59.8%
O 1s	25.2%	20.9%	24.7%	22.2%
N 1s	6.3%	7.6%	5.4%	6.8%
Ti2p	-	-	3.2%	1.8%
Si 2p	7.4%	8.4%	6.3%	8.0%
F 1s	-	-	1.5%	1.4%

Figure 4 a-b and Table 2 present survey spectra of GO+APTES and GO+APTES+$Ti_3C_2T_x$ before and after heating with the percentage of each element in the obtained materials, respectively. According to high-resolution C 1s spectra, after heating at 140°C for 5 hours in the vacuum oven, the intensity of the C=O and COOH peaks decreased, suggesting reduction of the amount of carboxylic groups in the hybrids.

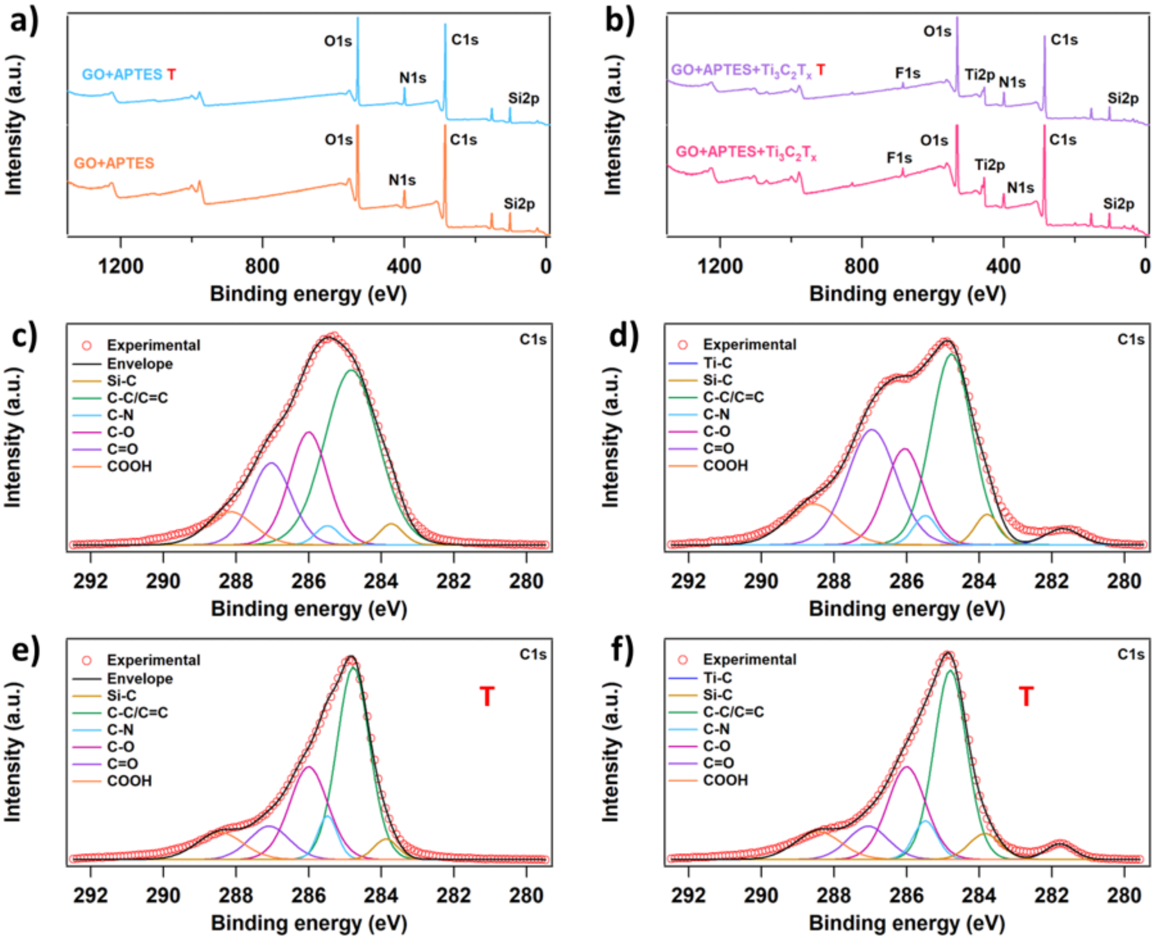

Figure 4. Comparison of XPS survey spectra of: a) GO+APTES and b) GO+APTES+ $Ti_3C_2T_x$ before and after heating at 140°C, 5h. High-resolution XPS spectra of: c) C 1s GO+APTES; d) C 1s GO+APTES +$Ti_3C_2T_x$; e) C 1s GO+APTES 140°C, 5h; f) C 1s GO+APTES +$Ti_3C_2T_x$ 140°C, 5h. "T" means heating at 140°C in the vacuum oven.

The electrochemical characterization of these materials is included in the Deliverable 2.3. Electrochemical characterization of electrode/electrolyte interfaces.

4 Production and characterization of ionic liquid prefilled electrodes

As part of task T2.2, SOLV has explored the IL prefilling of different Greencap electrode materials (CG and $Ti_3C_2T_x$). To achieve this, SOLV will used its internal knowledge and experience to produce these electrodes with AC[*]. The added value of these electrodes compared to conventional processes includes:

- Elimination of electrode drying steps
- Elimination of flammable solvents during electrode production
- Improved materials performances using pure ILs.

The use of pure IL electrolytes (without solvents) allows for greatly enhanced safety features (non-flammability), a wider range of operating temperatures and easier electrode production processes. All these benefits aim to reduce costs and allow the integration of supercapacitor cells in applications where the operating temperature, safety or recyclability are paramount.

In deliverable D2.2, the feasibility of employing this technique to produce electrodes with this methodology is detailed.

4.1 Curved graphene

4.1.1 Curved graphene/PTFE electrodes

In the initial stage of this study, electrodes of CG and AC were produced without IL prefilling as to compare the characteristics of these two materials. For this, polytetrafluoroethylene (PTFE) was used as a binder. Two electrode materials were produced *via* a conventional production method using ethanol as a solvent. In this process, the active materials (AM), PTFE and ethanol were mixed for 24 hours then the ethanol was partially removed *via* evaporation leaving a solid which can be worked and rolled into an electrode material. A ratio of 95%wt AM and 5%wt PTFE was used for both electrodes,

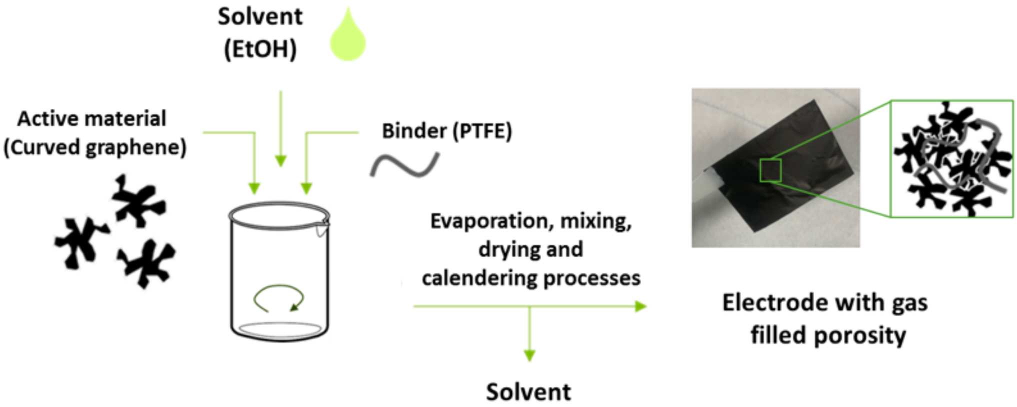

Figure 5. Production of CG/PTFE electrode.

---

[*] Method and apparatus for making electrodes for an ionic liquid-based supercapacitor, and method for making such a supercapacitor. **WO2020260444**

see Figure 5.

In comparison to AC, CG exhibits increased brittleness and rigidity, which leads to faster stiffening of the electrode paste during preparation. As a result, electrode fabrication became more challenging, particularly during the calendaring process, where maintaining mechanical integrity and avoiding structural damage proved difficult. Following multiple trials, electrode materials with comparable electrode loadings were obtained (8.99 and 9.07 mg/cm² for AC/PTFE and CG/PTFE respectively). These electrodes have significantly different thicknesses: 0.23mm for AC/PTFE and 0.12mm for CG/PTFE, due to the higher density of the CG compared to the AC (0.76 vs 0.39 g/cm^3).

These electrode materials were then assembled into the three-electrode Swagelok® cells in a symmetrical configuration (silver wire pseudo-reference electrode) and cycled using cyclic voltammetry (CV) with N-propyl-N-methylpyrrolidinium *bis*(fluorosulfonyl)imide (Pyr$_{13}$FSI) electrolyte and a GFA separator between 0 and 2.2V at a slow scan rate (10 mV/s), see Figure 6. A low cycling speed and low potential were chosen simply to avoid any redox reactions that could occur at higher potentials or current densities. The cell composed of AC-based electrodes presents lower resistance to charge/discharge as characterised by the square shape of the CV. On the other hand, the cell composed of CG-based electrodes presents a more resistive charge discharge profile, as indicated by the more oval shape. The working potentials on each electrode is similar for both cells. On the negative electrodes, working potential (ΔE_{neg}) of 1.23 to 1.29V are measured whereas working potential (ΔE_{pos}) of 0.91 to 0.97V are measured on the positive electrode. This suggests that, at a later stage of development, electrode mass balancing may be required as to equalize these electrodes working potential thus limiting the degradation of the electrodes.

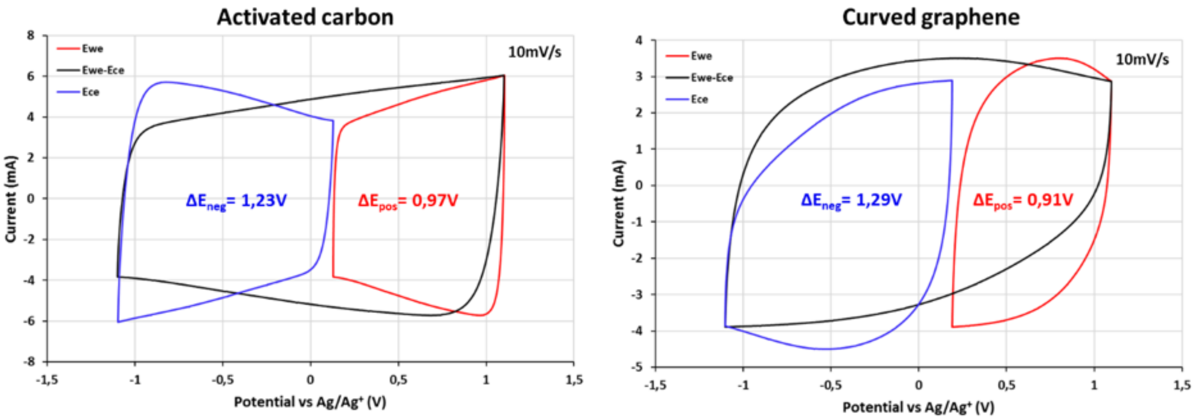

Figure 6. CV profile of cells composed of CG/PTFE (right) and AC/PTFE (left) electrodes, Pyr$_{13}$FSI electrolyte and GFA separator in Teflon Swagelok cells with a Ag wire reference. 0-2.2V; 10mV/s; symmetrical active mass; 11 mm electrodes; Pt current collectors.

When calculating the specific capacitance with respect to the weight of active materials, it was found that the AC has a much higher capacitance (27.7 vs 16.7 F/g). However, when looking at the volumetric capacitance, CG has a slightly higher value of 12.6 F/cm^3 with respect to AC (10.8 F/cm^3), see. We suggest that this difference could be partly explained by the differences in carbon structures. As other partners have also observed, the electrodes obtained with these materials differ in density (0.76 g/cm^3 for GC and 0.39 g/cm^3 for AC). This difference in density can explain the difference in capacitance between the active materials. Indeed, the higher density of the CG could limit the electrolyte penetration into the structure, which could affect the cell performance (*i.e.*, increased resistance, decreased charge storage).

Table 3. Comparison between CG/PTFE and AC/PTFE properties

Electrode	Electrode Thickness (mm)	AM Loading (mg/cm²)	AM density (g/cm³)	Cell specific capacitance (F/g)	Cell volumetric capacitance (F/cm³)
CG/PTFE	0.12	9.07	0.76	16.7	12.6
AC/PTFE	0.23	8.99	0.39	27.7	10.8

Given the results above, the production of IL prefilled electrodes is favourable to enhance electrolyte/electrode proximity and improve cell performance. Encouragingly, AC and CG behave similarly with respect to the process SOLV uses when producing electrodes suggesting that IL-prefilling is feasible.

4.1.2 Proof of concept: $Pyr_{13}FSI$ prefilled CG electrodes

Using the procedure described in SOLV's patent, the production of electrodes of CG and $Pyr_{13}FSI$ was attempted, see Figure 7. The IL $Pyr_{13}FSI$ was chosen as the starting point thanks to the high stability of this IL. When incorporating $Pyr_{13}FSI$ into the electrode material, no stiffening is observed leading to an easier electrode production compared to the abovementioned CG/PTFE electrodes. The electrode resembles a gel-like material which is very flexible and slightly moist. The CG electrode can uptake large amounts of IL (68 %) which is positive. Special attention was required when adding IL as this resulted in the electrode ripping during calendaring. The 95/5 CG/PTFE (%wt) ratio was maintained for this leading to an overall composition of 30/2/68 CG/PTFE/$Pyr_{13}FSI$ (%wt). In this production run, electrodes with a thickness of 0.21mm were produced. This corresponds to a loading of 9.10 mg/cm². This high loading is comparable to commercial loadings for AC-based supercapacitors. This electrode was characterised electrochemically (see D2.3) and delivered to CNR for further analysis.

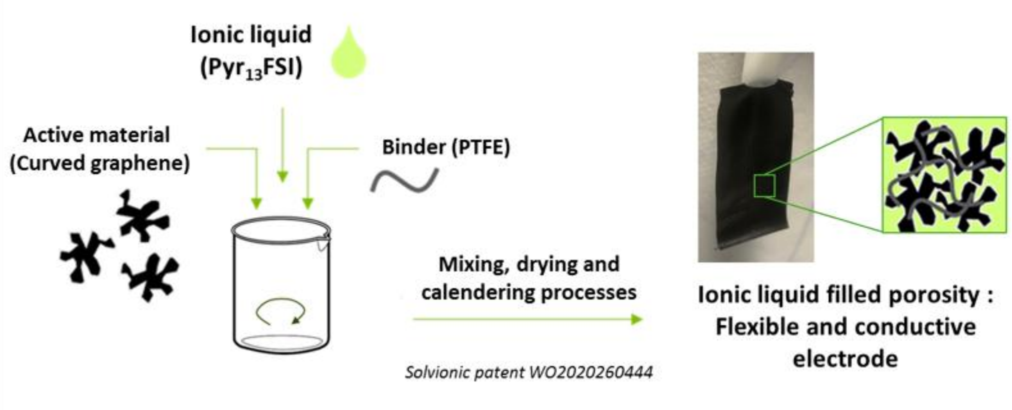

Figure 7. Production of IL prefilled CG/PTFE/Pyr13FSI electrode

4.1.3 Identification of optimal IL for CG prefilling

Although electrodes of CG were successfully produced with $Pyr_{13}FSI$, this IL may not be the most adapted for CG in terms of capacitance. Thus, a wide range of ionic liquids were produced and tested with the CG/PTFE electrode material using the same CV based methodology as described above. In total, 14 ionic liquids were tested with a variety of anions and cations of different sizes and chemistries. The highest capacitance values were obtained with EMImFSI. In these tests, it was observed that higher viscosity generally led to lower capacitance, see Figure 8. The exact chemical compositions of other ILs are withheld for confidentiality reasons.

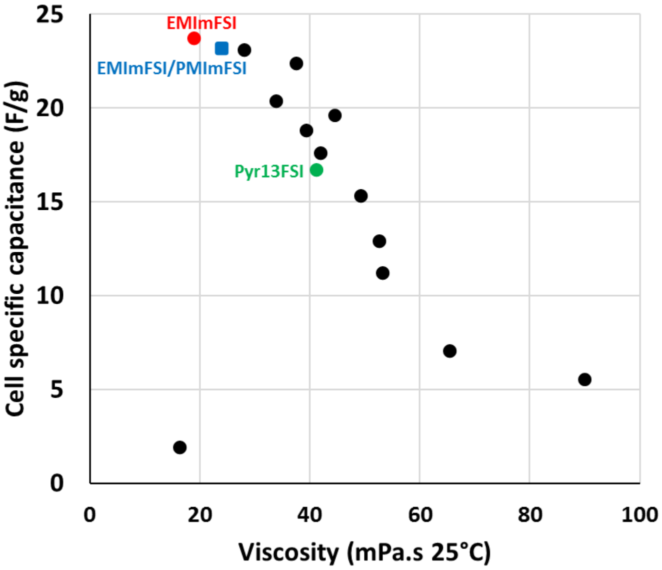

Figure 8. Variation of cell specific capacitance (F/g) as a function of electrolyte viscosity at 25 °C. Cell specific capacitance (vs active materials) of supercapacitor devices composed of CG/PTFE electrodes with different IL electrolytes. Measured by cyclic voltammetry (0-2.2V; 10mV/s); GFA separator; three electrode Swagelok cell; Ag wire reference; symmetrical active mass; 11mm electrodes; Pt current collectors.

Despite the high capacitance and low viscosity of EMImFSI, this IL will not allow the completion of the O3.3 because of its melting point of -14°C. To unlock the low temperature potential of this IL, mixtures of EMImFSI and other ILs were investigated as to identify eutectic composition that present no crystallisation down to -50°C (evaluated by differential scanning calorimetry (DSC)). The interaction between the ILs in an eutectic composition can modify their properties, such as lowering the melting point below that of the individual ILs. SOLV has previously developed electrolytes based on Pyr14FSI and OIP13FSI using this methodology for carbon nano tube and onion-like carbon electrodes[1]. Among the investigated mixtures, the 50/50 %wt mixture of EMImFSI and PMImFSI was selected as it presents no phase transitions down to -50°C and low viscosity (23.9 mPa.s at 25°C), close to the pure EMImFSI (19.4 mPa.s at 25°C), see Figure 9.

The EMImFSI/PMImFSI eutectic mixture was hence used to produce CG prefilled IL electrodes.

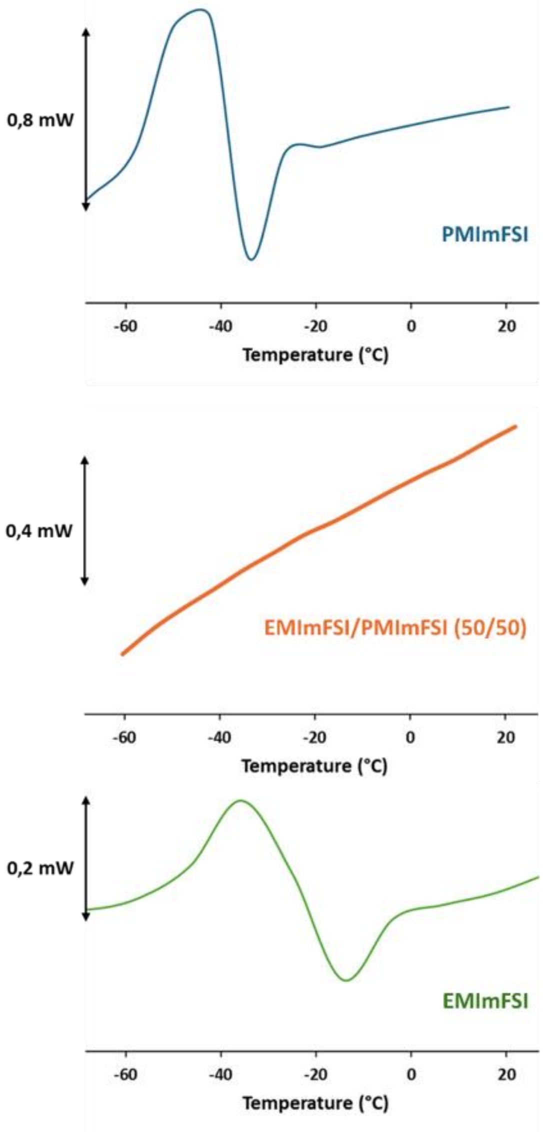

Figure 9. Differential scanning calorimetry of PMImFSI (top), EMImFSI/PMImFSI (middle) and EMImFSI (bottom) upon heating from -80 to 25 °C in inert atmosphere. Data taken from 3rd heating/cooling cycle at 5°C/min with aluminium pans.

4.1.4 Production of optimised electrodes: EMImFSI/PMImFSI prefilled CG electrodes

Using the same procedure used to produce CG/PTFE/Pyr$_{13}$FSI electrodes, electrodes were formulated with the EMImFSI:PMImFSI (1:1 mol) eutectic. These electrodes present the same properties in terms of aspect and flexibility compared to the Pyr$_{13}$FSI filled CG electrodes. Similar thickness (0.18mm) and loadings (9.22 mg/cm² in active materials) were obtained allowing for good comparison of these materials. This electrode was characterised electrochemically (see D2.3) and will be sent to UNISTRA for further development.

4.1.5 The characterization of CG/PTFE/Pyr$_{13}$FSI electrode

CNR-ISM SpecX Lab performed an experimental analysis of the structural and electronic properties of electrodes synthesized by SOLV, namely 30/2/68 CG/PTFE/Pyr$_{13}$FSI (%wt). Points of specific interest were the determination of chemical composition and mixing of the materials at the microscopic scale and the origin of the gradual decrease in capacitance and coulombic efficiency of the electrodes during electrochemical (charge/discharge) cycles. These points were addressed by photoemission spectroscopy (PES) and X-ray diffraction (XRD) measurements on CG/PTFE/Pyr$_{13}$FSI electrodes (supported by aluminum foil) cycled as detailed in Table 4**.**

Table 4. Description of the electrochemical cycles for the analyzed electrodes.

Electrode name	Applied voltage (V)	Specific current (A/g)	Number of cycles
TB275	2.8	0.5	10000
TB271	2.8	0.5	500
TB270	2.8	0.5	50
TB274	3.2	0.5	500
TB283	3.2	1.0	500

The positive and negative parts of the electrodes were labelled with the “+” and “-” signs.

The electronic structure of the electrodes was analyzed by PES with use of synchrotron radiation. The experiments were performed at the VUV-Photoemission beamline of the synchrotron Elettra (Trieste, Italy). The valence band was probed with 50 eV photon energy (hν), which provides high energy resolution (30 meV) and high sensitivity to the valence states. The chemical analysis was conducted at hν = 750 eV in order to acquire all relevant core level lines under the same experimental conditions.

Figure 10 reports the valence band spectra for all analyzed electrodes. The bottommost spectrum (yellow line) refers to a CG/PTFE electrode without ionic liquid. If compared to the spectrum just above (as-prepared CG/PTFE/Pyr$_{13}$FSI reference electrode, red line), it is evident that the valence levels are totally different. This observation, along with the well-known fact that the probing depth of PES at hν = 50 eV is in the order of about 1 nm, allows to state that the IL fills intimately the porosity of CG. The microscopic picture of the CG/PTFE/Pyr$_{13}$FSI electrode is that of CG grains separated by Pyr$_{13}$FSI. This morphological structure is negligibly modified by the electrochemical cycles. In fact, the lineshape of all other spectra in Figure 10 turns out to be very similar to that of the red spectrum. The only appreciable difference is the energy position of each spectrum, which shows positive or negative shifts (noted in the figure) with respect to the reference electrode. The shifts originate from changes in the crystallinity of the CG domains (see the XRD analysis below) and the formation of defects also in Pyr$_{13}$FSI, which pin the Fermi level of Pyr$_{13}$FSI at different position depending on the electrochemical cycle conditions. Considering the three topmost pairs of spectra in Figure 15 (same applied voltage and specific current but different number of cycles), it is possible to conclude that electrodes TB270 (50 cycles) and TB271 (500 cycles) represent a transient situation, while electrode TB275 (10000 cycles) is in a steady state, with very similar TB275^{+} and TB275^{-} spectra. Electrode TB283 shows the same behavior of electrode TB275, although with different cycling parameters. The negative shift observed in both cases (about -0.35 eV) can be considered an absolute (indirect) measurement of the defect density of the CG domains under stable working conditions. Finally, the comparison between electrodes TB283 and TB274 shows that higher specific current accelerates the achievement of steady-state conditions.

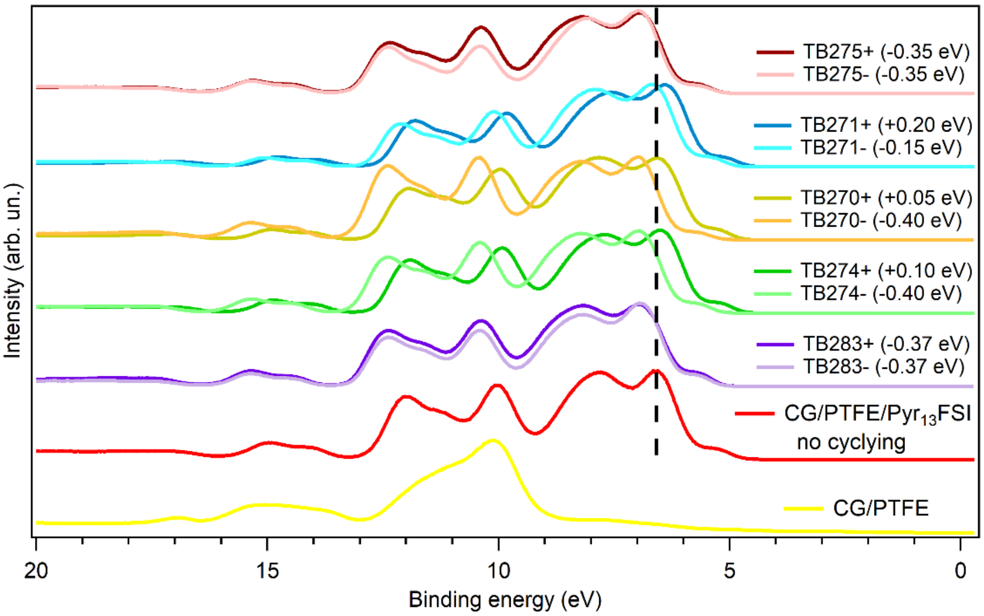

Figure 10. Valence band spectra of all analyzed electrodes.

The valence band analysis reported above finds confirmation in the core level data. Figure 11 reports the survey spectrum and the O 1s, N 1s, C 1s, and S 2p core level spectra (F 1s not displayed) for the CG/PTFE/Pyr$_{13}$FSI reference electrode. All photoemission peaks can be clearly associated to Pyr$_{13}$FSI, while there is no evidence of CG (graphitic carbon in CG ha binding energy 284.40 eV). Again, this indicates that Pyr$_{13}$FSI fills completely the porosity of CG.

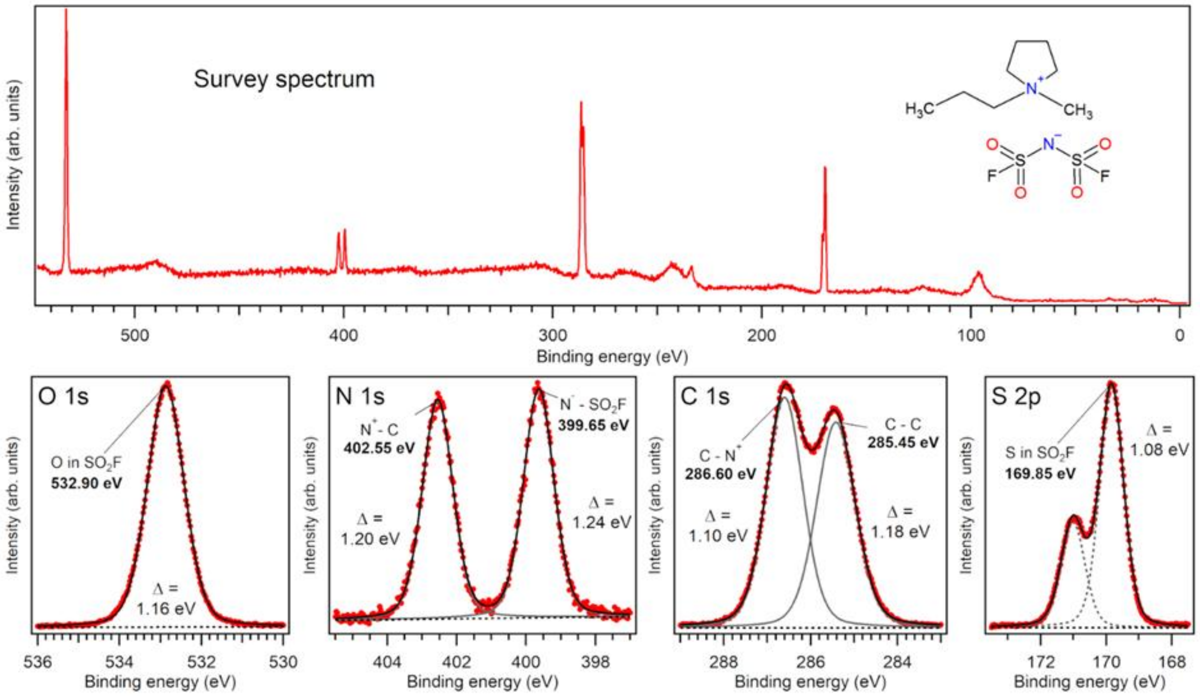

Figure 11. Survey and core level spectra of the CG/PTFE/Pyr$_{13}$FSI reference electrode

The electrochemical cycling leads to changes in the core level spectra that are coherent to those observed in the valence band. As an example, Figure 12 displays the survey and core level spectra of the TB283$^-$ electrode (the TB283$^+$ electrode shows very similar properties). All core level peaks are found at higher binding energies (0.25-0.35 eV) with respect to the reference electrode. Additionally, the width of the photoemission peaks (full width at half maximum Δ) has increased upon cycling by about 25% for all elements. This indicates clearly that the electrochemical cycles degrade the crystalline order of the electrode materials. Shifts of the core levels by the same amount and sign of the corresponding valence states and increased width of the photoemission peaks are observed for all electrodes.

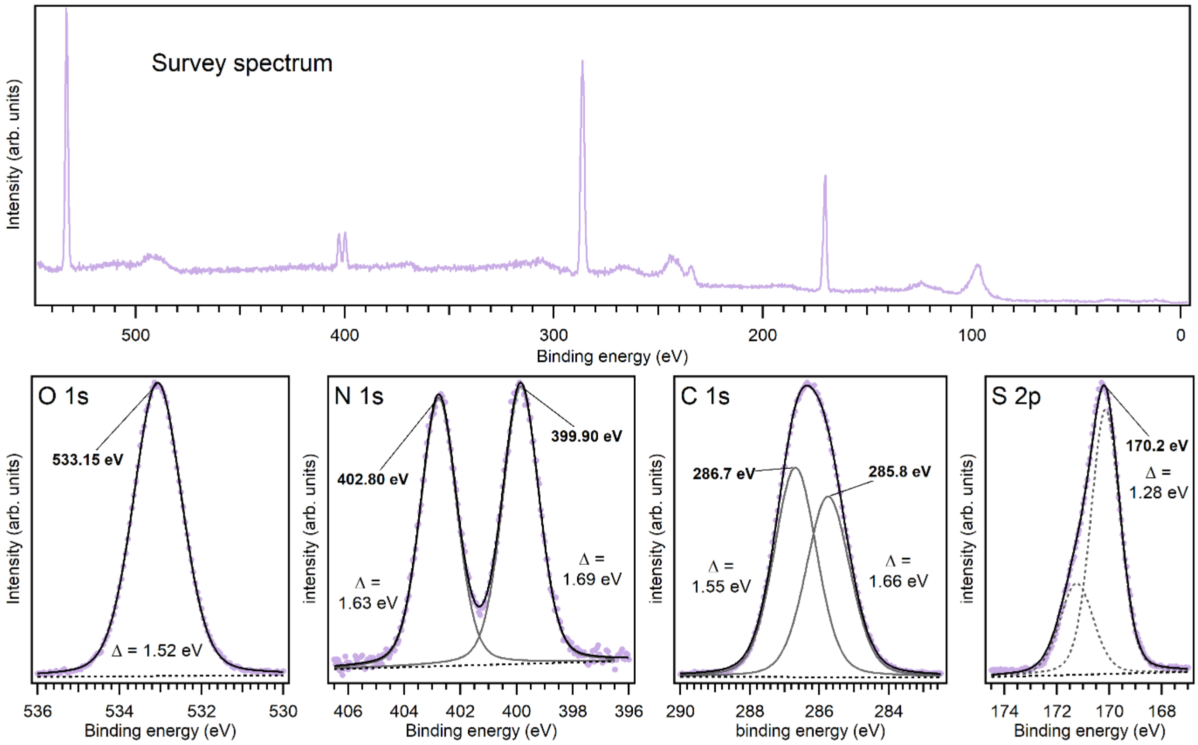

Figure 12. Survey and core level spectra of the TB283- electrode.

XRD measurements were conducted in Bragg-Brentano geometry using a PANalytical Empyrean diffractometer equipped with a PixCel 3D detector operating in linear mode, and a Cu-anode X-ray tube as the source. The samples were mounted on a custom-designed flat sample holder.

As shown in Figure 13, summarizing the XRD results, all patterns exhibit crystalline features attributable to the aluminum supporting material, marked with red asterisks in accordance with JCDD card no. 96-900-8461.[2] In one particular sample, namely the TB270+ electrode (50 cycles), a minor crystalline contribution arising from the formation of $Al(OH)_3$ (identified by arrows in the figure) is observed and indexed by JCDD card no. 01-070-20338.[3]

Crystalline reflections corresponding to PTFE (100) and curved graphene (CG) (002) are detected at 2θ ≈ 18° and 27°, respectively, consistent with previous observations made for the CG/PTFE/$Pyr_{13}FSI$ reference electrode. This reference pattern is also included in Figure 13 for comparison (magenta trace at the bottom).

The $Pyr_{13}FSI$ IL does not contribute to any observable diffraction peaks, being amorphous as expected. Moreover, when electrodes are exposed to an increasing number of electrochemical cycles at fixed voltage and current densities (black lines in Figure 13), the intensity of the PTFE and CG reflections progressively diminishes. By the 10^4th cycle, the long-range crystalline order of both PTFE and CG becomes undetectable for the positive electrodes, XRD peaks being no longer observed.

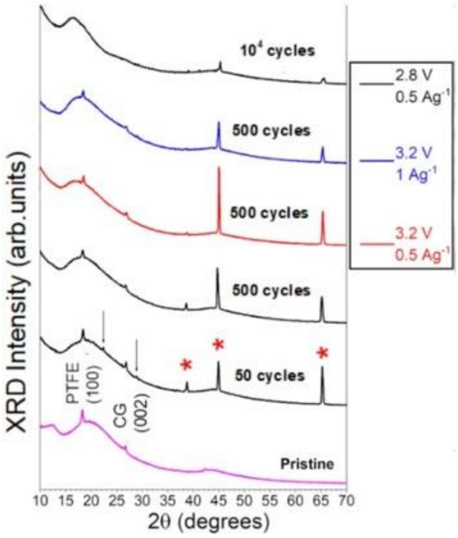

Figure 13. XRD patterns collected upon the differently cycled positive electrodes. Signals labelled by red asterisks are referred to the Al substrate, according to JCDD card nr. 96-900-8461.

This experimental evidence is well matching what previously discussed based on XPS measurements. Furthermore, varying the voltage and current densities while keeping the number of cycles constant (blue and red patterns) does not significantly affect the crystallinity.

To assess the reversibility or progression of the structural modifications induced by electrochemical cycling, the most affected electrode—specifically the TB275+ cycled 10^4 times— was re-examined after one month of storage in a glovebox. The corresponding results are displayed in Figure 14, which compares the XRD patterns of the as-received electrodes (red line) with the pattern collected after storage (black line). A recovery of the crystalline reflections is evident, suggesting that the structural changes induced by cycling are, to some extent, reversible.

In conclusion, the XRD characterization of cycled SOLV samples provide insights on the structural changes of electrodes working in different conditions. In particular, a crystallinity loss of both PTFE and CG is observed upon increasing the number of cycles. However, investigations conducted after one month of sample storage in a controlled glove box environment interestingly point out that the loss of structural order induced by working conditions appear not to permanently affect the electrodes.

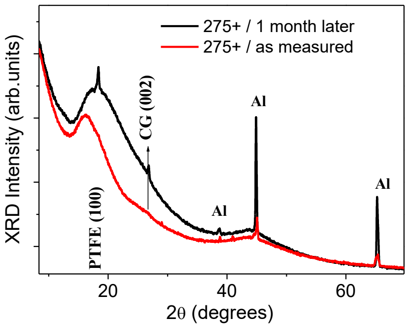

Figure 14. Comparison of XRD patterns collected upon as received electrodes (red lines) vs after one month of glove box storage (black lines).

4.2 MXenes ($Ti_3C_2T_x$)

Materials of Ti_3C_2Tx were received from TCD by SOLV. Electrochemical tests performed by partners demonstrated the promising performance of protic IL-based electrolytes with MXene electrodes. Given that the ILs developed for CG are aprotic (EMImFSI, PMImFSI, $N_{1113}FSI$, $Pyr_{13}BF_4$…), it was decided to produce a room-temperature protic IL for testing IL prefilling. For this, 1-ethylimidazolium bis(trifluoromethylsulfonyl)imide (EIHTFSI) was produced and purified as to achieve an electrolyte grade material, see Figure 15.

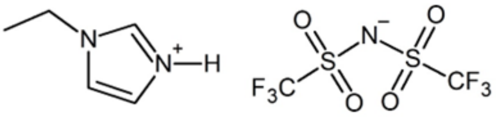

Figure 15. Structure of EIHTFSI

The production of MXene based IL filled electrode was first attempted using no binder. Indeed, as recommended by TCD, MXene can form electrodes without the need for binders. IL was added in small amounts to Ti_3C_2Tx whilst mixing and kneading. Proportions up to 75%wt in IL were tested. The particles of MXenes did not coalesce and at no point did a homogenous material form, see Figure 16. Next, the addition of PTFE was trialled. MXene and PTFE (aqueous dispersion) were initially mixed (90/10 MXene/PTFE (%wt)) then IL was slowly added. The material aggregated although, the particles of MXene refused to coalesce when rolling which lead to the expulsion of IL from the material. The final proportion of the material was 69.0/28.4/2.6 IL/MXene/PTFE. The amount of PTFE was then doubled (80/20 MXene/PTFE(%wt)) and the test repeated. Again, the MXene particles refused to merge. When attempting to calendar these materials, they ripped apart without stretching and the IL was pressed out, drying the material surface.

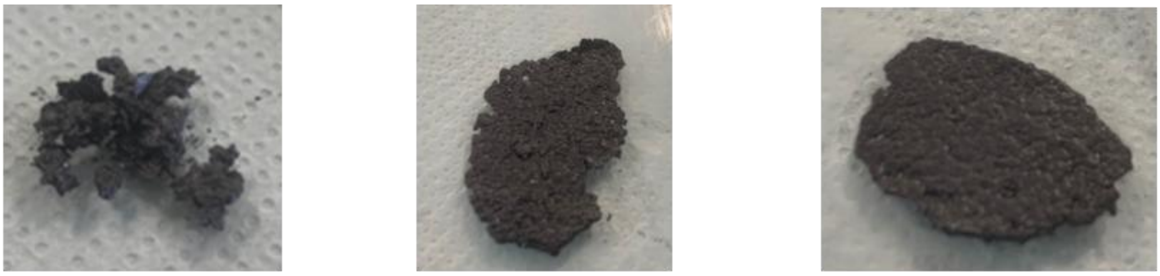

75,3% IL
24,6% MXene
0% PTFE

69,0% IL
28,4% MXene
2,6% PTFE

69,7% IL
24,8% MXene
5,4% PTFE

Figure 16. Aspect of materials obtained when attempted the production of EIHTFSI filled MXene electrodes.

In the conditions tested, IL-filled MXene electrodes were not produced with the same process as CG/IL/PTFE electrodes. The production of IL-filled MXene electrodes requires more development as to produce electrode material.

4.3 Structural properties of differently aged electrodes

CNR-ISM-SpecX Lab measured for BDM differently aged electrodes composed of AC, few graphene layers (FLG), 1-ethyl-3-methylimidazolium bis(fluorosulfonyl)imide ionic liquid electrolyte (EMIFSI) and carboxymethyl cellulose/styrene-Butadiene Rubber binder (CMC/SBR), deposited on carbon coated Aluminum substrates, where structurally characterized by means of XRD (same instrumentation/experimental conditions as previously reported). The aim was to investigate the relationship between the structural evolution of the electrode materials and the performance of the corresponding electrochemical cells.

The electrodes were subjected to different galvanostatic charge-discharge (GCD) cycling protocols as outlined below:

CELL #1: 50 GCD @ 0.5 A g-1 V= 2.7 V (Capacity retention~98%)

CELL #2: 500 GCD @ 0.5 A g-1 V= 2.7 V (Capacity retention~94%)

CELL #3: 2000 GCD @ 0.5 A g-1 V= 2.7 V (Capacity retention~87%)

CELL #4: 500 GCD @ 0.5 A g-1 V= 3.0 V (Capacity retention~85%)

CELL #5: 10000 GCD @ 0.5 A g-1 V= 2.7 V (Capacity retention~70%)

The corresponding XRD patterns are shown in Figure 17. Peaks corresponding to aluminum and aluminum oxide phases, originating from the substrate, are marked with asterisks and squares, respectively, based on JCPDS card no. 00-001-1177 and JCPDS card no. 00-005-0712. Additionally, the diffraction peaks of highly crystalline FLG are identified, with reflections observed at 2θ = 27° (002) and 2θ = 54° (004), in excellent agreement with the literature.[4]

No features related to crystalline CMC/SBR[5] or EMIFSI were detected, suggesting a predominantly amorphous nature of these components.

Regardless of the number of cycles, FLG consistently retained its crystalline structure, with no evidence of strain or stress induced by cycling. Comparative analysis of cells, from CELL#1 to CELL #4 revealed crystallization and oxidation of the CMC/SBR binder, as indicated by characteristic reflections marked with red and black arrows, respectively, a fact supported by previous studies.[6] These effects became more pronounced with increasing cycle number and applied voltage. On the other hand, for CELL#5 only a slight, almost negligible, presence of crystalline CMC/SBR can be observed as the complete crystallization is not reached. Furthermore, no evidence of CMC/SBR oxidation was found in this case upon cycling. Notably, CELL#5 also lacked signals associated with native aluminium oxide phases, suggesting that both the crystallization and oxidation of CMC/SBR are assisted by the presence of Al_2O_3.

In conclusion in samples CELL#1 to CELL#4, where oxidation of the aluminium substrate (formation of native Al_2O_3) is evident, prolonged cycling led to both crystallization and oxidation of the CMC/SBR binder, indicating electrode degradation. Conversely, the electrode from CELL#5, which did not exhibit aluminium oxidation and underwent 10,000 cycles, showed negligible crystalline CMC/SBR features only. These findings suggest that CMC/SBR crystallization is not solely a result of extended cycling-induced degradation, but is closely associated with the presence of native aluminium oxides.

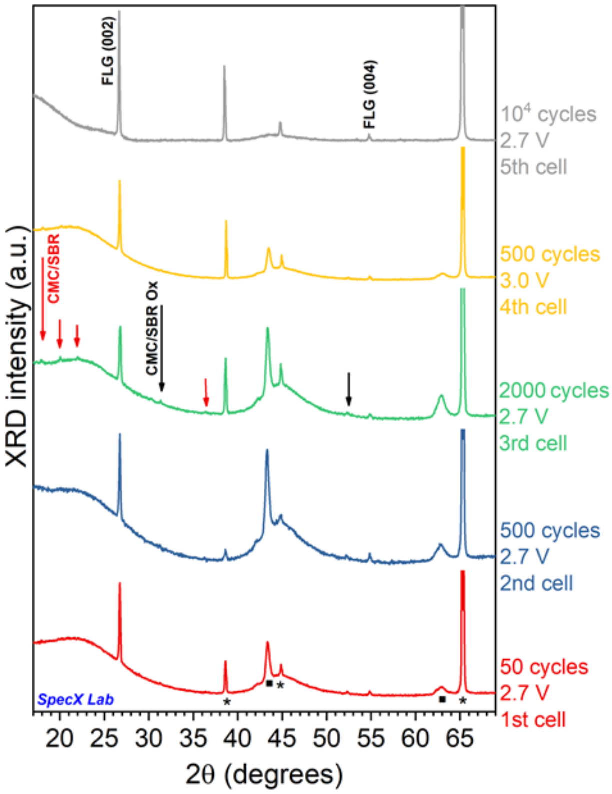

Figure 17. XRD patterns collected upon differently cycled electrodes: CELL#1 (red line); CELL#2, (blue line); CELL#3 (green line); CELL#4 (yellow line); CELL#5 (grey line).

5 Functionalization of graphene with diazonium compounds

UCAM performed 4-Nitrobenzenediazonium tetrafluoroborate (4NBD) functionalization on HPH graphene. The reaction between graphene and the diazonium group in 4NBD occurs spontaneously at room temperature. The schematic of the process is in Figure 18. Graphene and 4NBD were dispersed in DI water and sonicated to ensure the reaction occurs homogenously throughout the sample. The processed graphene was subsequently characterised using Raman spectroscopy, atomic force microscopy (AFM), scanning electron microscopy (SEM), and energy-dispersive X-ray spectroscopy (EDX).

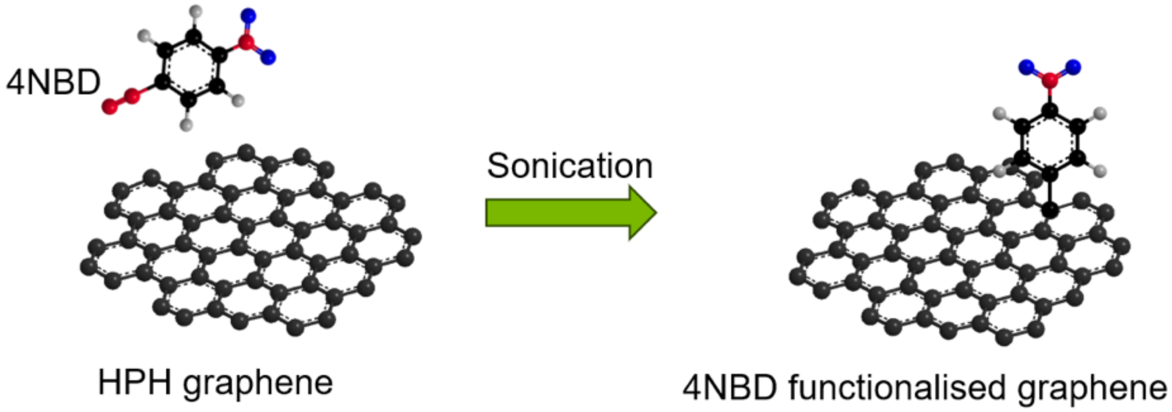

Figure 18. Schematic of 4NBD-functionalized HPH graphene

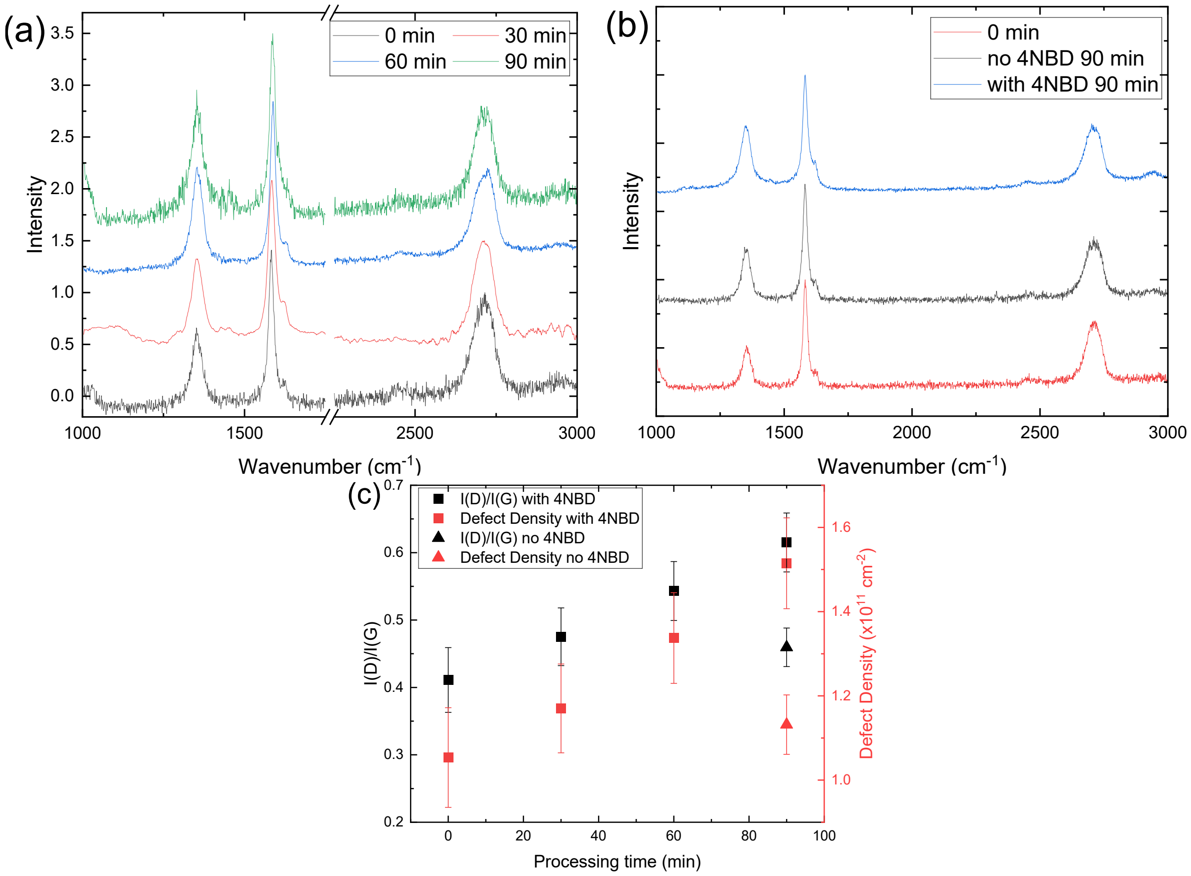

Figure 19. a) Raman spectra of samples processed with 4NBD for different durations from 0 to 90 min. b) Raman spectra of sample sonicated for 90 min with and without 4NBD. c) I(D)/I(G) and defect density for different processing durations.

Figure 19a shows Raman spectra of samples processed with 4NBD for different reaction times from 0 to 90 min. I_D increases with processing time. Since both the chemical reaction with 4NBD and sonication can contribute to the increase in defects, UCAM further investigated the relative contributions of defects from these two factors. Samples were processed by sonication without the addition of 4NBD for 90 mins to estimate the increase in defect due to sonication. The resulting Raman spectra are in Figure 19b. The sample without 4NBD also showed an increase in I_D. The overall change in I_D/I_G and the calculated defect density are in Figure 19c and Table 5. From Table 5, it is estimated that the 4NBD processing increased the defect density by 4.61 x 10^{10} cm^{-2}, while sonication alone by 0.78 x 10^{10} cm^{-2}. Therefore, the reaction with 4NBD caused an increase in defects of up to 3.83 x 10^{10} cm^{-2}.

Table 5. I_D/I_G and defect densities for samples processed with sonication for 90 min with and without 4NBD

	I_D/I_G	Defect Density ($x10^{11}$ cm^{-2})	Increase in Defect Density ($x10^{10}$ cm^{-2})
HPH Graphene	0.411 ± 0.05	1.05 ± 0.12	-
4NBD 90 min sonication	0.615 ± 0.04	1.51 ± 0.11	4.61 ± 0.19
No 4NBD 90 min sonication	0.460 ± 0.03	1.13 ± 0.07	0.78 ± 0.23

UCAM also characterised the 4NBD functionalized graphene using AFM. Figure 2a shows an AFM image of the functionalized graphene. The height profiles of several individual flakes were also measured as represented by the white line. Figure 19b shows the height profiles of 3 individual functionalized graphene flakes. The flake thicknesses were found to be between 3 to 5 nm, which is similar to the flake thicknesses before functionalization.

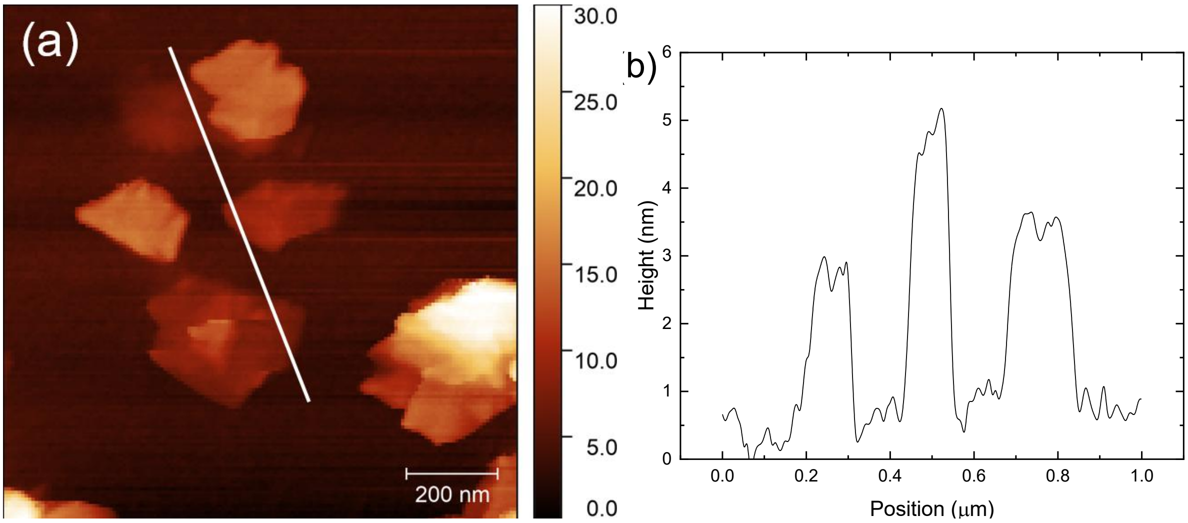

Figure 20. a) AFM image of HPH graphene processed with 4NBD for 90 min. b) Height profile along the white line in a) passing through 3 graphene flakes.

UCAM also characterised the functionalized graphene using SEM/EDX to check the flake elemental composition. EDX spectra were taken over a large area as shown by the SEM image in Figure 20a to estimate of the elemental composition. Figure 3b is the EDX spectrum and the elemental composition is in Table 6. The spectrum shows a small N peak~0.39 eV which confirms the addition of

N due to the 4NBD functionalisation. This corresponded to 2at% N in the sample after 90 min of processing time. A slightly larger oxygen peak was also observed, due to the presence of the -NO_2 nitro group in the covalently attached 4NBD and the cellulose binder added during the HPH process, before functionalization. The total oxygen content was estimated to be 5.8 at%, among which ~4% from the nitro group due to its stoichiometry with N, and the remaining 1.8% due to the cellulose binder used.

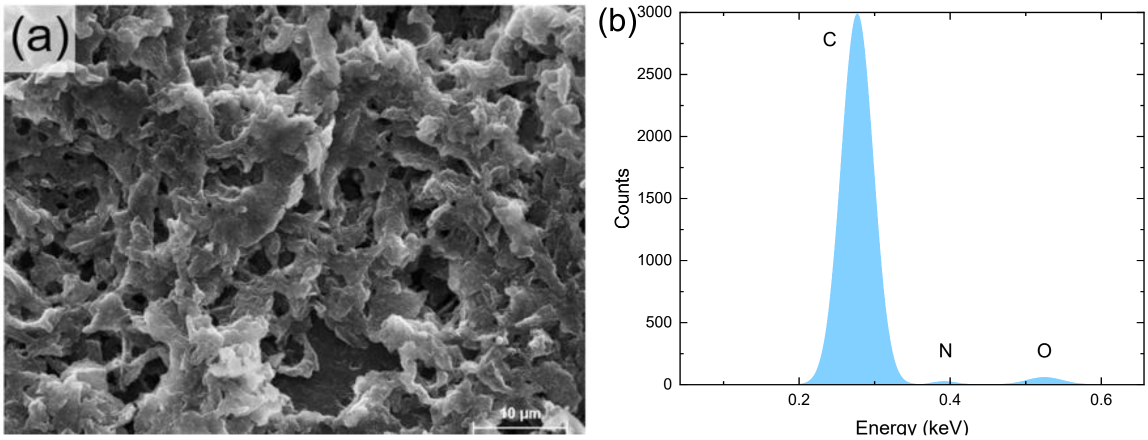

Figure 21. a) SEM image of 4NBD functionalized HPH graphene. b) EDX spectrum

Table 6. Atomic composition of 4NBD functionalized HPH graphene

Element	Series	Atomic concentration (%)
C	K-series	92.2
N	K-series	2.0
O	K-series	5.8

UCAM characterised the sheet resistance of films made by functionalized graphene to check that the functionalization did not detrimentally change the conductivity. As a standard, films with 25 µm thickness were fabricated. The functionalized graphene was dispersed into DI water to form an ink, then blade-coated onto a glass substrate. The height of the sample was characterised by a profilometer as shown in Figure 22. The sample was then characterised using a 4-point probe. The resultant sheet resistance is in Table 7 with comparison to that of unfunctionalized graphene. This shows that functionalized graphene is still highly conductive, with a sheet resistance of 5.5 Ω/□, meeting the required KPI ≤ 100 Ω/□.

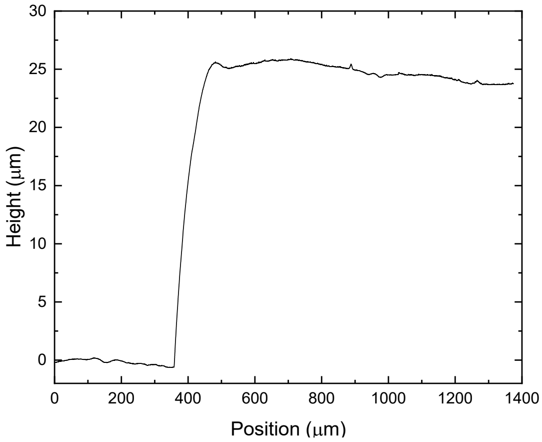

Figure 22. Height profile of functionalized graphene film on glass.

Table 7. Sheet resistance and conductivity of 4NBD functionalized and unfunctionalized samples.

Material	Sheet Resistance (Ω/□)	Conductivity (S/m)
4NBD functionalized graphene	5.5	7273
HPH graphene	4.1	9756

6 Functionalization of MXene with azobenzene sulfonic acid

TUD conducted covalent functionalization of V_2C with 4-aminoazobenzene-4'-sulfonic acid sodium salt (ASA) as a starting molecule (Figure 23 a). The amino group of starting compound was first converted to a diazonium salt ($-N_2^+Cl^-$) by reaction with $NaNO_2$ and HCl in an iced bath, whereas sulfonic acid sodium salt underwent conversion into sulfonic acid in the strong acidic environment. The V_2C dispersion was next added to the diazonium salt solution in an iced bath. When the reaction reached room temperature, the diazonium group dissociated from the molecule, generating radical compounds that subsequently bonded with electronegative surface terminals of V_2C MXene (Figure 23 b). The grafted organic molecule was expected to confer multiple benefits to the K^+-storage performance of V_2C, such as a redox-active nature for the additional K^+-storage site.

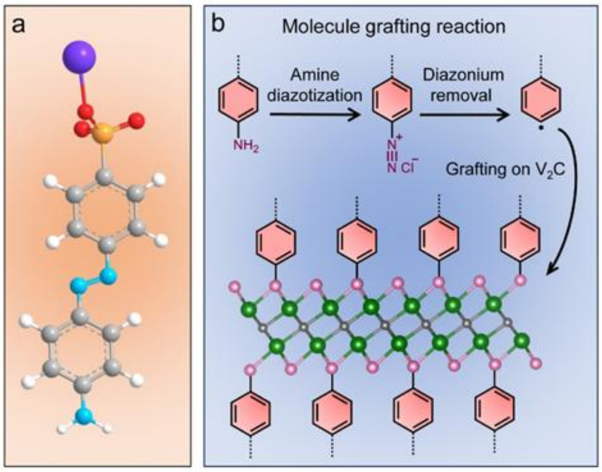

Figure 23. a) 4-aminoazobenzene-4'-sulfonic acid sodium salt (white sphere: H; grey sphere: C; blue sphere: N; orange sphere: S; red sphere: O; purple sphere: Na). b) Schematic representation of functionalization of V_2C MXene (black sphere: C; green sphere: V; pink sphere: the terminals of V_2C MXene).

According to SEM image, the obtained ASA-V_2C nanoflakes display a noticeably curved morphology (Figure 24 a), while the high-resolution transmission electron microscopy (HR-TEM) (Figure 24 b and c) revealed the significant increase of the interlayer distance from 0.86 nm to 1.25 nm from the pristine V_2C film to ASA-V_2C, respectively. The XRD patterns (Figure 24 i) further confirmed these data as (002) reflex shifted towards lower 2Θ after functionalization, *i.e.* from 10.3° (0.86 nm) to 7.9° (1.12 nm) and 7.1° (1.25 nm) for V_2C MXene, BP-V_2C, and ASA-V_2C, respectively indicating the increase of the interlayer distance.

The thermogravimetric analysis (TGA) analysis of BP-V_2C and ASA-V_2C revealed the stable grafting of organic molecules until a high temperature of 259°C (Figure 24 d). It was estimated that the organic molecule accounts for 8.3% and 9.1% of the total weight of BP-V_2C and ASA-V_2C, respectively. Fourier transform infrared (FT-IR) spectra shows characteristic peaks of phenyl units, including aromatic C=C stretching (1474 cm^{-1}) and aromatic C-H in-plane bending (1010 and 1086 cm^{-1}) for both BP-V_2C and ASA-V_2C. In addition, the peak of ASA-V_2C at 1119 cm^{-1} confirms the presence of sulfonic acid group ($-SO_3H$ stretching, while its N=N stretching (1474 cm^{-1}) overlaps with aromatic C=C stretching. These results further confirm the successful functionalization of V_2C MXene (Figure 24 e).

Moreover, XPS was performed to evaluate the oxidation of V_2C before and after functionalization (Figure 24 f-h). In the V 2p XPS spectrum of pristine V_2C, four deconvoluted peaks can be detected, corresponding to V $2p_{1/2}$ peaks of V^{4+} (523.8 eV) and V^{2+}/V-C (520.9 eV), as well as V $2p_{3/2}$

peaks of V^{4+} (516.3 eV) and V^{2+}/V-C (513.4 eV). The presence of high-valence V^{4+} indicates surface oxidation of V_2C. In comparison with V_2C, ASA-V_2C shows a much weaker V 2p XPS signal, while the signal is even marginal for BP-V_2C. This observation suggests dense and homogeneous coverage of functional molecules on the V_2C surface. Following 20 keV Ar^+ cluster sputtering for 5 min, the V 2p signal intensity of BP-V_2C and ASA-V_2C become substantially enhanced. Both BP-V_2C and ASA-V_2C show dominant V^{2+}/V-C peaks, and their high-valence V^{4+} peaks are considerably suppressed. This result reflects the effective role of the grafted molecules in inhibiting surface oxidation of V_2C.

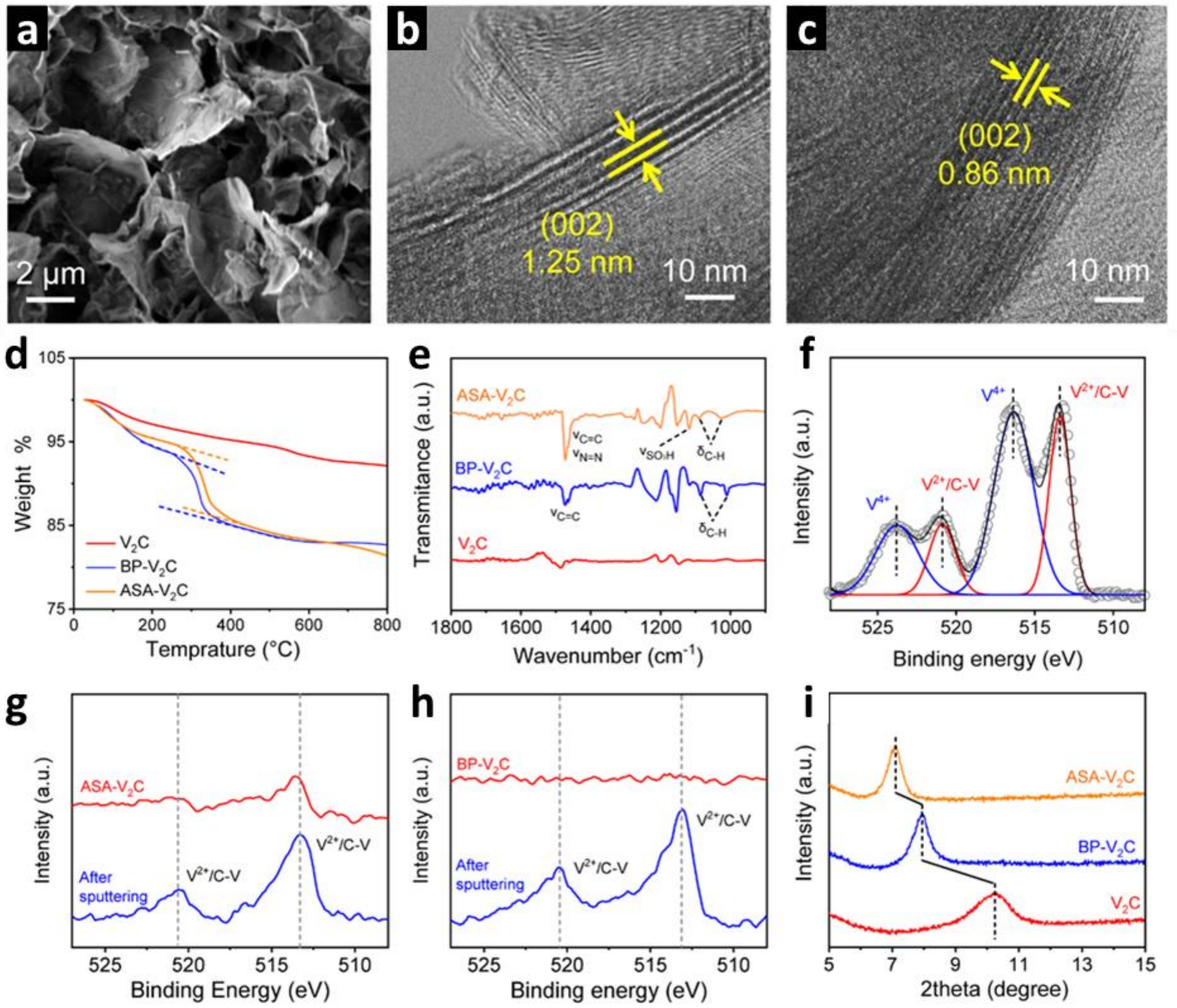

Figure 24. a) SEM image of ASA-V_2C nanoflakes. HR-TEM images of: b) the ASA-V_2C film and c) the pristine V_2C film. d) TGA and e) FT-IR spectra of V_2C, BP-V_2C, and ASA-V_2C. High-resolution V 2p XPS spectra of: f) V_2C, (g) BP-V_2C, and h) ASA-V_2C. i) XRD patterns of V_2C, BP-V_2C, and ASA-V_2C.

7 Hybridization of CG with FLG

The conventional EMs consisted in the hybridization of the CG, provided by SKL, with BED FLG. Different mass ratios between the active material (CG) and the conductive agent (FLG) were considered and compared to the state-of-the-art (SoTA) electrode formulation, in order to achieve the best performances in term of specific capacitance and rate capability. Moreover, the substitution of the SoTA polyvinylidene binder (PVDF) with CMC-SBR has been considered. The materials were characterized by scanning electron microscopy and through four-probe conductivity experiment. The mixing procedure is deeply described in D3.1.

At BED the morphological characterization of the conventional electrodes is carried out by SEM analysis, and it is shown in Figure 25. Both AC-based and CG-based slurry (Figure 25 a,b) exhibit similar grain sizes (under 10 µm), with the latter showing a denser morphology which is further enhanced by the substitution of both CB and PVDF with FLG and CMC/SBR, respectively. Specifically, a clear morphological change is shown in the direction of a less disordered and compacted structure. In fact, CB exhibits a disordered and voluminous features, which disappear after its substitution with FLG.

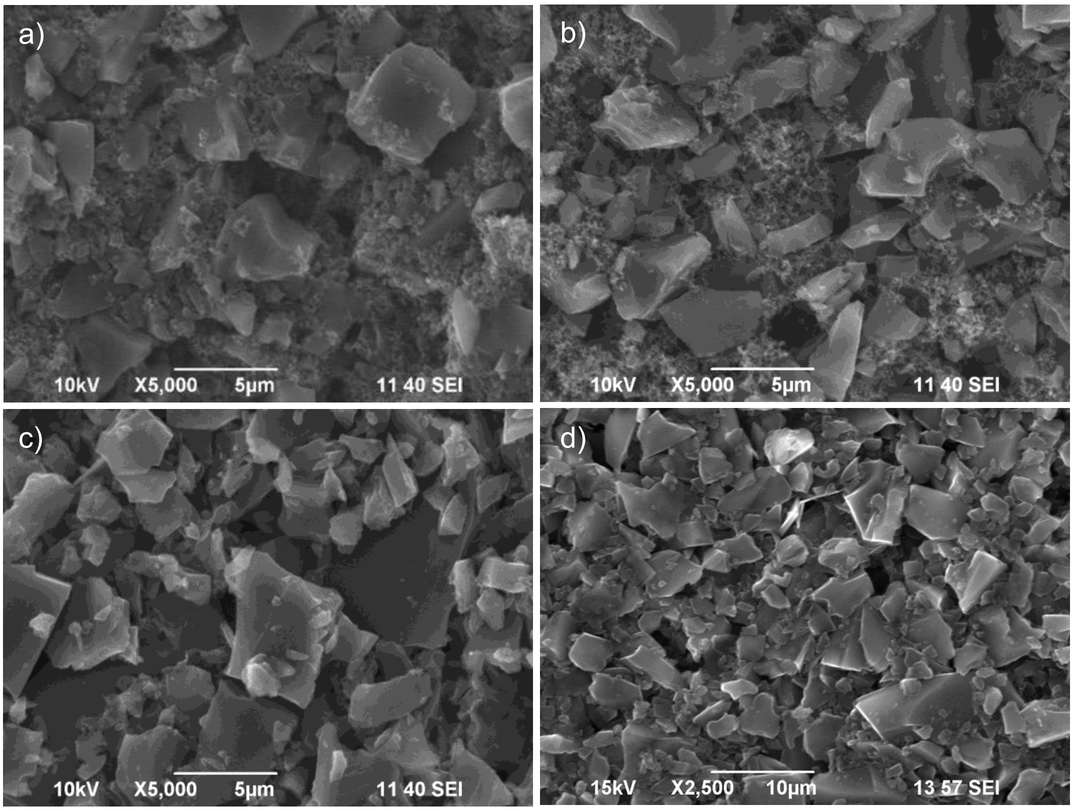

Figure 25. *SEM imaging of the slurries. a) AC-CB-PVDF; b) CG-CB-PVDF; c) CG-FLG-PVDF; d) CG-FLG-CMC/SBR.*

The presence of FLG favour a more efficient packaging and interconnection of carbon flakes, resulting in a lower resistivity (Figure 26a) and an higher specific energy as a function of the specific power (Figure 26b). Specifically, the resistivity drops widely after the substitution of AC with CG attesting the superior conductivity of CG with respect to the former. The conductivity is further improved by the addition of FLG, reaching the lowest value of (240 ± 10) mΩ×cm which translates in a sheet resistance of (30 ± 4) Ω/□ for an indicative 80 µm thick slurry. By the substitution of PVDF with CMC-SBR the resistivity and the sheet resistance are increased to (273 ± 5) mΩ×cm and to (34 ± 2) Ω/□, respectively. The slurry obtained with CMC-SBR widely reach the sheet resistance (R_s < 100 Ω/□) and the sustainability targets for the EMs, being eco-friendly and PFAs-free. In conclusion, the synergy between

CG and FLG is beneficial for the electrode conductivity enabling to lower the content of the conductive additive itself needed for keeping a low equivalent series resistance (ESR), thus maximizing the active material, as shown in D3.1.

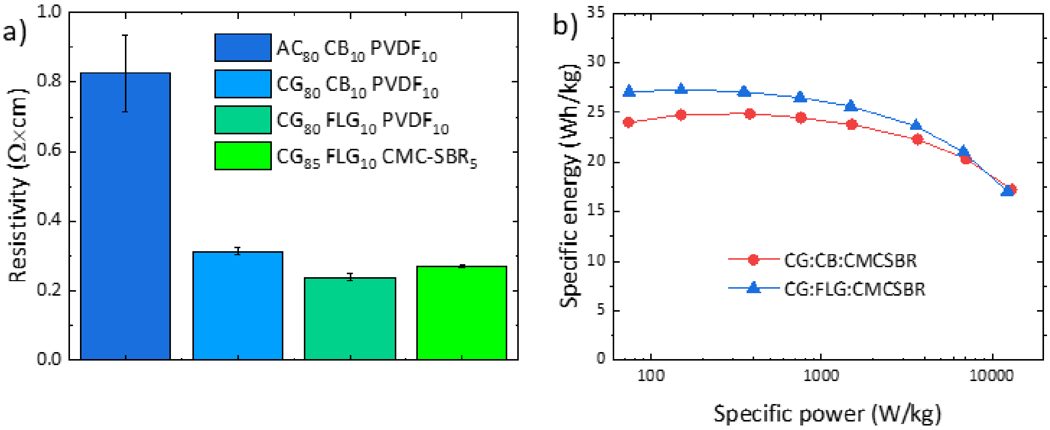

Figure 26. *a) Resistivity of the slurries based on different electrode material compositions. b) Ragone plot of CG-FLG and CG-CB based electrodes. Performance Improvement by the substitution of CB with FLG.*

8 Ionogel-based electrodes

Furthermore, BED investigated the hybridization of the electrode materials with ILs, producing IGs-based electrodes following an adapted method of the SOLV patent (Patent no. WO2020260444 A1). Specifically, AC and FLG were used as the active material and the conductive additive, respectively. The IL employed was EMIFS) (Figure 27). The specific procedure followed for the production of IGs electrodes is deeply described in D3.1 is recalled by the figure below for the reader convenience.

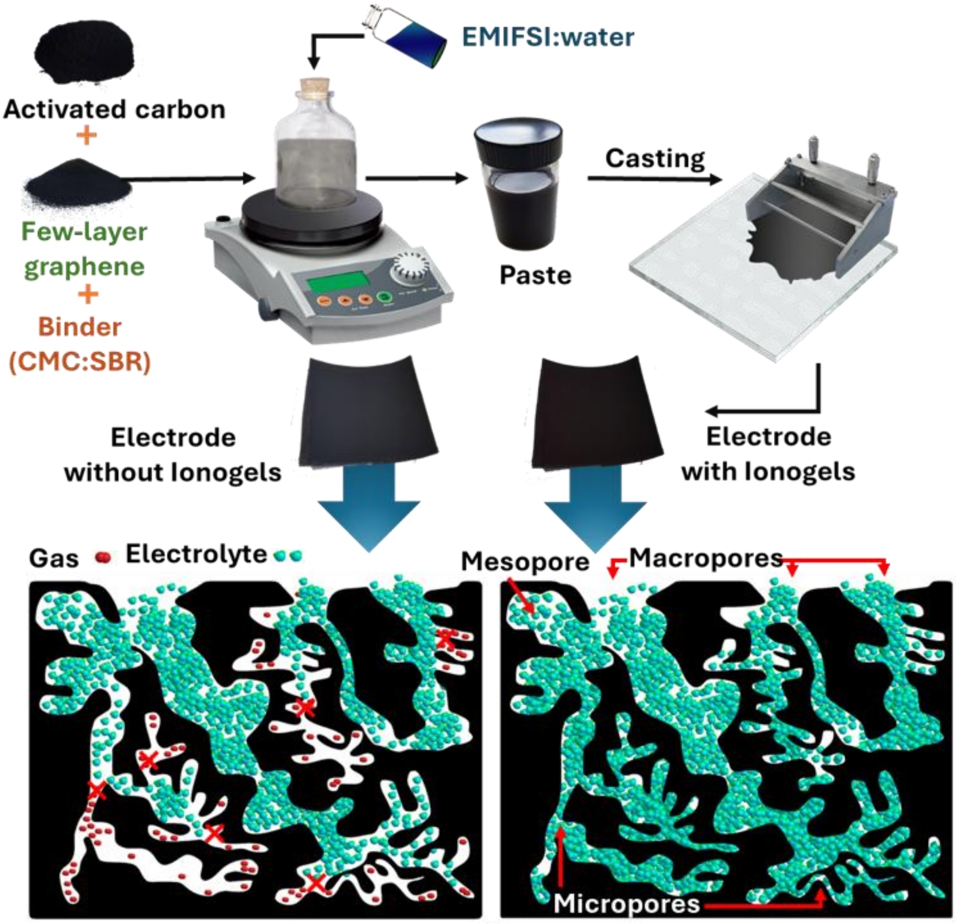

Figure 27. *Preparation procedure of the IGs-based (right) and conventional electrodes (left). Below it is schematized the electrodes pores wetting with and without the IGs-based method.*

BED tested the IGs-based electrodes in CV and with GCD. In comparison with conventional electrodes based on the same formulation, the IGs-based electrical double layer capacitor (EDLC) exhibits a lower ESR as qualitatively suggested from the CV curve initial slopes (Figure 28a). In fact, the IGs-based EDLC has a superior rate capability performance, retaining more than 80 % of initial capacity after a 100 time increment the specific current, while the conventional EDLC almost halved its initial specific capacity (Figure 28b) in the same specific current range. Such outstanding behaviour might be attributed to the improved wetting of the electrode surface by the IL, obtained during the electrode slurry fabrication.

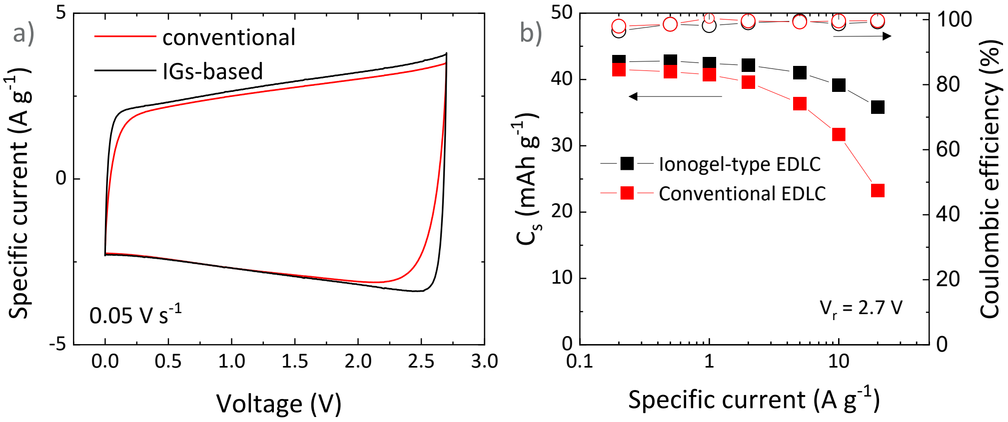

Figure 28. *a) CV curve of conventional and IGs-based EDLC. Voltage rate: 50 mV/s. Electrolyte: EMIFSI. b) Specific capacity and coulombic efficiency as a function of the current rates for the conventional and IGs-based EDLC. Electrolyte: EMIFSI.*

9 Conclusion and Recommendation

This deliverable summarizes the progress achieved within Work Package 2 of the GREENCAP project, which is focused on the development of functionalized and hybrid EMs based on 2DMs for SC applications. The overarching objective was to enhance electrochemical performance through strategic structural design, surface modification, and electrolyte integration, with a strong emphasis on the use of CRM-free and sustainable components.

UNISTRA led the synthesis and hybridization of rGO and $Ti_3C_2T_x$ MXene, including both physical mixing and covalent functionalization using APTES. These hybrid materials exhibited improved interfacial compatibility and textural properties. **BED** focused on the hybridization of CG with FLG, demonstrating improved electrode integrity, porosity, and electrolyte access. **UCAM** conducted functionalization of graphene using 4NBD diazonium chemistry, successfully increasing the defect density and tailoring surface reactivity. Parallel work by UCAM on V_2C functionalization with sulfonated azobenzene derivatives further advanced MXene tuning strategies.

TCD and **SOLV** collaborated on the integration of ILs into EMs. ILs such as EMImFSI and PMImFSI were tested in IG configurations. While CG-based IG electrodes were successfully produced and demonstrated stable performance, MXene-based IG electrodes faced processing challenges, including poor cohesion and IL expulsion. These results indicate the need for further optimization of IL-MXene systems, potentially through binder modification or alternative structuring approaches.

CNR-ISM contributed to the structural and electrochemical characterization of aged electrodes composed of FLG, AC, and IL electrolytes. XRD analyses provided insights into the effects of cycling on binder crystallization and substrate interaction. Notably, the crystalline stability of FLG was preserved over long-term cycling, whereas evidence of CMC/SBR degradation was correlated with the presence of Al_2O_3.

Overall, the hybridization and functionalization approaches explored in WP2 have proven effective in improving the electrochemical and structural properties of 2DM-based electrodes. The integration of ILs, while promising in the case of CG, requires further development for MXene systems. The insights gained here provide a solid foundation for material scale-up and integration in full cell devices under WP3 and WP4.

Recommendations

- Continue optimization of rGO/MXene and CG/FLG hybrid systems to improve electrical conductivity, ion transport, and mechanical integrity.
- Refine IL-prefilled electrode fabrication, particularly for MXene-based IGs, by evaluating binder ratios, mixing techniques, and calendarability.
- Deepen aging studies to identify degradation mechanisms in binders and substrates; develop strategies to mitigate these effects.
- Expand chemical functionalization to further tailor interfacial properties between EMs and ILs, especially under high-voltage and high-temperature conditions.

The work in D2.2 demonstrates meaningful progress toward GREENCAP’s mission to deliver sustainable, high-performance, and CRM-free SCs. The collaborative efforts across partners—including UNISTRA, BED, UCAM, TCD, SOLV, and CNR-ISM—underline the strength of the consortium and provide a strong technological base for the next project phases.

10 Risks and interconnections

10.1 Risks/problems encountered

No risks have arisen related to this deliverable.

Risk No.	What is the risk	Probability of risk occurrence[1]	Effect of risk[1]	Solutions to overcome the risk
WP2.2.	Problem with functionalization of graphene and MXenes	M	H	Optimization of reaction conditions (time, solvent, temperature); change the compound used for functionalization
WP2.2.	Problem with preparation of stable dispersions of prepared materials	M	H	Longer sonication time; change of solvent
WP2.2.	Problem with preparation of IL-filled MXene electrodes	M	H	Optimization of parameters (*e.g.*, ratio, solvent, binders)

1) Probability risk will occur: 1 = high, 2 = medium, 3 = Low

11 References

[1] R. Lin, P.-L. Taberna, S. Fantini, V. Presser, C. R. Pérez, F. Malbosc, N. L. Rupesinghe, K. B. K. Teo, Y. Gogotsi, P. Simon, *J. Phys. Chem. Lett.* **2011**, *2*, 2396-2401.

[2] R. W. G. Wyckoff, *Crystal Structures, Vol. 1*, **1963**.

[3] H. Saalfeld, M. Wedde, *Z. Kristallogr.* **1974**, *139*, 129-135.

[4] X. Wang, L. Zhang, *RSC Adv.* **2019**, *9*, 3693-3703.

[5] B. Yin, G. Li, D. Wang, L. Wang, J. Wang, H. Jia, L. Ding, D. Sun, *Adv. Polym. Technol.* **2018**, *37*, 1323-1334.

[6] aN. Haleem, M. Arshad, M. Shahid, M. A. Tahir, *Carbohydr. Polym.* **2014**, *113*, 249-255; bW. Chen, J. Gu, S. Xu, *Express Polym. Lett.* **2014**, *8*; cT. Anjali, *Carbohydr. Polym.* **2012**, *87*, 457-460.

12 Acknowledgement

The author(s) would like to thank the partners in the project for their valuable comments on previous drafts and for performing the review.

Project partners:

#	Partner short name	Partner Full Name
1	BED	BEDIMENSIONAL SPA
2	SOLV	SOLVIONIC
3	FSU	FRIEDRICH-SCHILLER-UNIVERSITAT JENA
4	SKL	SKELETON TECHNOLOGIES OU
5	TCD	THE PROVOST, FELLOWS, FOUNDATION SCHOLARS & THE OTHER MEMBERS OF BOARD, OF THE COLLEGE OF THE HOLY & UNDIVIDED TRINITY OF QUEEN ELIZABETH NEAR DUBLIN
6	TUD	TECHNISCHE UNIVERSITAET DRESDEN
7	UNISTRA	UNIVERSITE DE STRASBOURG
8	SM	SKELETON MATERIALS GMBH
9	UNR	UNIRESEARCH BV
10	CNR	CONSIGLIO NAZIONALE DELLE RICERCHE
11	UCAM	THE CHANCELLOR MASTERS AND SCHOLARS OF THE UNIVERSITY OF CAMBRIDGE
12	CU	Y CARBON LLC

Disclaimer/ Acknowledgment

This project has received funding from the European Union's Horizon Europe research and innovation programme under grant agreement No 101091572. Views and opinions expressed are however those of the author(s) only and do not necessarily reflect those of the European Union. Neither the European Union nor the granting authority can be held responsible for them.